Seawater δ^7Li: a direct proxy for global CO_2 consumption by continental silicate weathering?

Christoph Wanner[1], Eric L. Sonnenthal[1] and Xiao-Ming Liu[2,3]

[1]*Earth Sciences Division, Lawrence Berkeley National Laboratory, 1 Cyclotron Road, Berkeley CA, 94720, USA.*

[2]*Geophysical Lab, Carnegie Institute of Washington, Washington D.C., 20015, USA.*

[3]*Department of Geology, University of Maryland-College Park, College Park, MD, 20742, USA.*

ABSTRACT

The fractionation of stable Li isotopes (^{6}Li, ^{7}Li) has become a promising proxy for assessing changes related to continental silicate weathering patterns. Recently, the first complete record of Cenozoic seawater Li isotopic composition (δ^7Li) was reported (Misra and Froelich, 2012, Science 335, 818-821) showing a stepwise increase of +9‰ over the last 56 Ma. This increase was attributed to a general change in continental silicate weathering behavior caused by tectonic uplift. In particular, the low global average riverine δ^7Li inferred for the Paleocene-Eocene boundary was explained by congruent silicate weathering of primary silicate minerals, which is inconsistent with the stoichiometry of secondary minerals and the resultant water chemistry.

In this study, we present a novel reactive transport modeling approach that explicitly includes Li isotopic fractionation to assess alternative geochemically-constrained interpretations that do not rely on congruent weathering. Simulations show that riverine δ^7Li is mainly controlled by the subsurface residence time, the corresponding weathering intensity, and the

concentration of a river's suspended load. Based on these factors, we suspect that the low δ^7Li observed at the Paleocene-Eocene boundary was inherited from a high weathering intensity with predominant weathering of previously formed secondary mineral phases (e.g., clays, oxides) having low δ^7Li values. Moreover, we conclude that the Cenozoic δ^7Li increase was caused by an increasing amount of primary silicate mineral dissolution inherited from an increasing suspended river load concentration and a decreasing weathering intensity both likely induced by tectonic uplift. In contrast, Cenozoic cooling and corresponding pCO_2 and precipitation variations do not seem to have a distinct control on the Cenozoic δ^7Li record.

Finally, our simulations revealed a close relation between δ^7Li and CO_2 consumption by silicate weathering implying that the Cenozoic seawater δ^7Li record could be potentially used to quantify such CO_2 consumption through time. However, more experimental and modeling work is required to quantify the correlation between seawater δ^7Li and global CO_2 consumption by silicate weathering. Key parameters are the temperature-dependent thermodynamic properties of specific Li-bearing primary and secondary minerals (e.g., crystallographic Li substitution reaction, maximum Li substitution, Li solubility, Li isotopic fractionation factor) as well as the determination of global average subsurface and river discharges through time.

1. INTRODUCTION

Continental chemical weathering forms a major CO_2 sink and is therefore an important input parameter for climate models (e.g., Berner and Kothavala, 2001; Berner et al., 1983; Francois and Godderis, 1998; Godderis et al., 2009; Li and Elderfield, 2013). However, the present and past global CO_2 consumption by continental silicate weathering has not been precisely quantified (Li and Elderfield, 2013). Climate models simulating the carbon cycle over

Earth's history typically calibrate CO_2 consumption by chemical weathering against the observed seawater $^{87}Sr/^{86}Sr$ ratio. Using $^{87}Sr/^{86}Sr$ is challenging because it reflects chemical weathering of carbonates, as well as weathering of silicate minerals (Godderis et al., 2009; Oliver et al., 2003). Tracking the individual contribution of continental silicate weathering is, however, crucial because it may demonstrate whether an observed global CO_2 drawdown is caused by increased tectonic activity, such as the onset of the Himalayan orogeny ca. 30 Ma years ago (Raymo and Ruddiman, 1992), or by a decrease in total Earth CO_2 degassing (Berner et al., 1983). In contrast to Sr, lithium is a trace element that is almost exclusively found in silicate minerals, which makes it a useful tracer for silicate weathering (e.g., Huh et al., 2001; 1998; Kisakürek et al., 2005; 2004; Liu et al., 2013; Millot et al., 2010; Pogge von Strandmann et al., 2010; 2006; Rudnick et al., 2004; Vigier et al., 2009). In particular, tracking Li isotopic fractionation is promising because the two stable Li isotopes (^{6}Li, ^{7}Li) fractionate when Li-bearing primary silicate minerals (e.g., micas) are weathered and secondary mineral phases (e.g., clays) are formed (Pistiner and Henderson, 2003; Vigier et al., 2008; Wimpenny et al., 2010; Zhang et al., 1998).

Hathorne and James (2006) presented the first record of seawater Li isotopic composition ($\delta^{7}Li$) over the past 18 Ma years using foraminifera as a proxy. Misra and Froelich (2012) extended the record to 68 Ma showing a +9‰ increase over the last ca. 56 Ma. Unlike the steady $^{87}Sr/^{86}Sr$ increase, $\delta^{7}Li$ increased stepwise, which was attributed to specific tectonic events (e.g., Himalayan orogeny) (Misra and Froelich, 2012). Specifically, the latter authors argued that tectonic uplift shifted the global silicate weathering pattern from a congruent, transport-limited regime to an incongruent, weathering-limited regime. However, the latter interpretation cannot be fully justified from a geochemical perspective, because secondary minerals typically observed

69 under a transport-limited weathering regime (e.g., Fe- and Al-oxides) are inconsistent with
70 congruent silicate weathering.

71 Among the earth sciences, reactive transport modeling has become a powerful tool for a
72 predictive understanding of many subsurface systems (Steefel et al., 2005). To the best of our
73 knowledge, it has not yet been used for a quantitative understanding of Li isotope fractionation
74 processes. Instead, field-derived Li isotopic data were usually explained by using closed system
75 Rayleigh distillation models (Kisakürek et al., 2004; Rudnick et al., 2004; Tipper et al., 2012;
76 Yoon, 2010). Such models greatly simplify Li isotope fractionation processes because they only
77 consider fractionation effects associated with the precipitation of Li-bearing minerals from an
78 aqueous solution having a specific initial Li concentration. In contrast, they neglect that aqueous
79 Li concentrations, and thus corresponding Li isotope fractionation effects, are also controlled by
80 the simultaneous dissolution of Li-bearing primary minerals. Recently, Bouchez et al. (2013)
81 presented a box-type mass balance and flux model that considers both dissolution of Li-bearing
82 primary minerals and the precipitation of Li-bearing secondary minerals. Similar to Rayleigh-
83 type models, the Bouchez et al. (2013) model does not take into account mineralogical, kinetic
84 and thermodynamic properties of mineral phases involved in Li isotope fractionation processes
85 (e.g., mineral stoichiometry, dissolution and precipitation rates, mineral solubilities).

86 In this paper we present a reactive transport modeling approach explicitly including the
87 fractionation of Li isotopes to quantitatively test alternative interpretations for the Cenozoic
88 seawater δ^7Li record that do not rely on congruent silicate weathering. By doing so, we show that
89 global average riverine and seawater δ^7Li values are mainly controlled by the cumulative extent
90 of water-rock interaction taking place along a flow path and are thus closely related to the
91 corresponding CO_2 consumption.

2. Global Li isotopic fractionation model

2.1. The Misra and Froelich (2012) model

Using a mass balance approach Misra and Froelich (2012) argued that the change in seawater δ^7Li was solely attributed to a change in riverine δ^7Li. The conclusion that changing seawater δ^7Li values are mainly caused by a changing fate of continental Li seems reasonable as there is evidence that the seawater hydrothermal fluid input and oceanic Li isotopic fractionation processes remained roughly constant during the Cenozoic (Müller et al., 2008; Rowley, 2002). However, the rate of past oceanic crust production is still under debate. For example, various GEOCARB models (e.g., Berner, 1994; Berner and Kothavala, 2001) consider a variable hydrothermal fluid input. Moreover, the low seawater δ^7Li values observed at the Paleocene-Eocene boundary (Misra and Froelich, 2012) could be inherited from a lower global average riverine δ^7Li value (at constant riverine Li flux), from a lower dissolved riverine Li flux (at a constant δ^7Li value), or from a combination of both. In fact, it is rather unlikely that processes causing a shift of the global average riverine Li isotopic composition do not vary the global average riverine Li flux and [Li].

It is well accepted that Li isotopic fractionation is mainly associated with secondary mineral precipitation (Kisakürek et al., 2005; Millot et al., 2010; Pogge von Strandmann et al., 2010; 2006; Vigier et al., 2009). By contrast, Li isotopes stoichiometrically dissolve from primary silicate minerals (Huh et al., 2004; Pistiner and Henderson, 2003). Riverine δ^7Li is thus controlled by the ratio of Li released by primary silicate mineral dissolution to Li removed by secondary mineral precipitation and by Li isotopic fractionation associated with precipitation.

Consequently, host rock mineralogy does not show a distinct control on riverine δ^7Li (Kisakürek et al., 2005; Millot et al., 2010). Changing global average riverine δ^7Li values thus reflect a changing silicate weathering pattern only.

For the Paleocene-Eocene boundary (~56 Ma ago) a global average riverine δ^7Li value of +3‰ was inferred (Misra and Froelich, 2012), being ca. 20‰ lower than the average δ^7Li value of modern rivers. Misra and Froelich (2012) concluded that this light value was inherited from congruent weathering of primary silicate minerals having a δ^7Li value in the same order of magnitude, whereas the current value is inherited from incongruent silicate weathering including secondary mineral precipitation (e.g., clays, oxides, and hydroxides) and accompanying Li isotopic fractionation. Whereas average continental bulk rock δ^7Li values close to +3‰ are justified by the studies of Teng et al. (2004; 2008; 2009) reporting δ^7Li values for the average (δ^7Li=+2.0±2.3‰), upper (δ^7Li=0±2‰) and lower continental crust (δ^7Li=+1.6±8.9‰), congruent silicate weathering seems rather questionable. Specifically, Misra and Froelich (2012) argued that the global weathering regime at the Paleocene-Eocene boundary was similar to the current low-relief, peneplained type and transport-limited weathering pattern inferred for the Guayana Shield (Edmond et al., 1995). The Guayana Shield is located at the border of Venezuela, Colombia and Brazil and one of the so far lowest riverine δ^7Li values was measured for a sample collected from this area (+6.6‰, Huh et al., 1998). Edmond et al. (1995) indeed characterized the weathering regime of the Guayana Shield as being weathering-intense and transport-limited but they explicitly stated that primary silicate minerals are incongruently dissolved. In fact, only incongruent silicate mineral dissolution can explain the formation of thick saprolites with an accumulation of quartz, clays, Fe- and Al-oxides typically observed at locations experiencing a high weathering intensity (Kisakürek et al., 2004; Liu et al., 2013;

Rudnick et al., 2004; White et al., 2001). Incongruent silicate weathering is also consistent with the low Al solubility at near neutral pH values, typical of these systems.

Furthermore, it is questionable if the average riverine δ^7Li value at the Paleocene-Eocene boundary was as low as +3‰. If this is true, similar riverine δ^7Li values should be found somewhere on Earth today reflecting weathering conditions for an isolated location that are similar to the global weathering pattern observed in the past (Hathorne and James, 2006). In fact, the compilation of available current riverine δ^7Li values showed that the minimum values were larger, on the order of 6‰ (Misra and Froelich, 2012). Values close to +6‰, however, have so far only been published for two specific samples and only one of them originated from a weathering intense location (Guyana Shield, Huh et al., 1998). The other sample was collected from a Siberian river (Yana) where the weathering intensity is lower (Huh et al., 1998). Nevertheless, it is notable that +6‰ is in the same order of magnitude as the asymptotic riverine δ^7Li value Misra and Froelich (2012) obtained for the Paleocene-Eocene ocean by performing a sensitivity analysis on their mass balance calculations. Based on this analysis, the lack of present river δ^7Li values less than +6‰, and a recent refinement of the Li cycle at the Paleocene-Eocene boundary ($\delta^7Li_{riverine}$=+12‰, Li and West, 2014), we propose that the Paleocene-Eocene riverine δ^7Li was likely around +6‰ or larger. Inferring a global average riverine δ^7Li that is higher than the value of the upper continental crust (δ^7Li=0.0±2‰, Teng et al., 2004) implies that Li isotopic fractionation between bulk crustal rocks and global rivers was taking place. Moreover, it rules out congruent weathering as being responsible for the minimum seawater δ^7Li observed at the Paleocene-Eocene boundary.

2.2. Alternative hypotheses explaining the Cenozoic seawater δ^7Li value record

Following the arguments of Misra and Froelich (2012), we assume that increasing Cenozoic seawater δ^7Li values are mainly attributed to a change in riverine δ^7Li. We do, however, not *a priori* assume that the riverine Li flux and the hydrothermal seawater Li input remained constant. Nevertheless, we focus on changing riverine δ^7Li values rather than possible effects of changing Li isotopic fractionation processes in the ocean (i.e., reverse weathering) and a variable seawater hydrothermal Li input. Also, we assume that the composition of the continental crust exposed to chemical weathering remained roughly constant since the Paleocene-Eocene boundary, thus neglecting potential effects of time-varying lithology on global average riverine and seawater δ^7Li values. Similar to Misra and Froelich (2012), we speculate that the Cenozoic seawater δ^7Li value increase is most likely inherited from a changing continental silicate weathering pattern induced by an increasing global relief owing to major global orogenies (e.g., Himalayan, Andean orogeny) and by the cooling trend observed since the humid Paleocene-Eocene thermal maximum (PETM) (Clementz and Sewall, 2011; Miller et al., 1987). An increasing relief (Fig. 1) and cooler temperatures have the following first order effects on chemical silicate weathering, which have potentially caused the observed δ^7Li shift:

1) An increasing relief shifts the hydraulic gradient to higher values, increasing flow velocities and shortening residence times along a specific subsurface flow path (Fig. 1). Cooler temperatures decrease the dissolution rates of primary silicate minerals (Lasaga, 1984). Hence, increasing relief and cooler temperatures limit water-rock interaction along specific flow paths.

2) For a low relief, such as inferred for the Paleocene-Eocene boundary (Misra and Froelich, 2012), the hydraulic gradient is low and the average subsurface residence time is high. Long residence times under hot and humid climatic

conditions (Clementz and Sewall, 2011; Miller et al., 1987) cause a high degree of water rock-interaction with plenty of newly formed secondary mineral phases, which is usually described as a weathering-intensive or transport-limited weathering pattern (Misra and Froelich, 2012). We thus assume that at the Paleocene-Eocene boundary, the global average saprolite thickness (composed of mostly quartz, clays, Fe- and Al-oxides) was higher than it is today (Fig. 1). Following this argument, and taking into account an increasing global relief as well as decreasing temperatures, the degree of exposure of the silicate bedrock to chemical weathering must have increased over the last 56 Ma, which is equivalent to proposing a decreasing weathering intensity. It should be noted that our use of "weathering intensity" throughout this paper strictly refers to the chemical index of alteration (CIA), which is the commonly used proxy for expressing the chemical weathering intensity of a particular rock or soil sample (Nesbitt and Young, 1982). This definition is particularly useful because it takes into account the ratio between immobile (e.g., Al) and mobile (e.g., Na, Ca, K) elements, on which the amount of newly formed clays, oxides and hydroxides has a first order control. Alternatively, riverine aqueous species concentrations (e.g., [Si], normalized [Si]) have been proposed to operate as weathering intensity proxies (Kisakürek et al., 2005; Pogge von Strandmann et al., 2006). The drawback of using riverine aqueous species concentrations is that, once chemical equilibrium is reached, their concentrations become discharge independent (Maher, 2011), whereas chemical silicate weathering fluxes and corresponding weathering rates are

linearly increasing with increasing discharge (Gaillardet et al., 1999; Maher, 2011). The strong dependence on discharge implies that also chemical silicate weathering rates do not necessarily correspond to weathering intensity. For instance, a relatively low chemical weathering rate was calculated for the weathering intense Guyana Shield (Gaillardet et al., 1999).

3) Owing to the higher hydraulic gradient, an increasing global relief shifts the physical erosion rate (i.e., denudation rate) to higher values (Bouchez et al., 2013). A higher denudation rate leads to an increase of the suspended river load concentration, as long as the suspended load is not deposited in lowland areas (Gaillardet et al., 1999; Milliman and Meade, 1983). Consequently, we speculate that the global average suspended river load concentration increased over the last 56 Ma such as already argued by Misra and Froelich (2012).

3. Methods

A series of thermodynamically- and kinetically-controlled reactive transport model simulations using TOUGHREACT V2 (Xu et al., 2011) were performed to assess the effect of the identified changing weathering parameters on Cenozoic global average riverine and seawater δ^7Li (i.e., decreasing subsurface residence time, cooling trend, decreasing weathering intensity, increasing suspended river load concentration). TOUGHREACT has been used to evaluate isotopic fractionation coupled to water-rock interaction and hydrological processes in a variety of subsurface environments and laboratory experiments (e.g., Singleton et al., 2005; Sonnenthal et al., 1998; Wanner and Sonnenthal, 2013).

3.1. Model Setup

Two different types of simulations were carried out to model silicate weathering and associated Li isotopic fractionation (i) in the subsurface and (ii) within rivers (Fig. 2).

3.1.1. *Subsurface simulations*

Reactive transport of infiltrating meteoric water along a typical subsurface flow path (e.g., arrows on Fig. 1) was simulated for a fully water-saturated, 200 m long porous media with an assumed porosity of 10%. The unsaturated zone was neglected because our focus was on assessing the sensitivity (i.e., trends) of dissolved δ^7Li values as a function of residence time, climate, and weathering intensity rather than on simulating detailed flow features of infiltration through the unsaturated zone and recharge to aquifers and rivers. Subsurface simulations were run for an average linear flow velocity of 1 m/d to simulate a system dominated by advection. The 200 m long model domain (Fig. 2) was divided into 200 cubic grid blocks of 1x1x1 m each to numerically solve the governing differential equations using TOUGHREACT's integral finite differences approach (Xu et al., 2011).

Pure water in equilibrium with atmospheric CO_2 was specified as initial and boundary fluid compositions. In doing so, atmospheric CO_2 is partially dissolved and provides H^+ necessary for silicate weathering reactions such as illustrated for the weathering of albite to kaolinite:

$$CO_{2(g)} + H_2O = HCO_3^- + H^+ \quad (1)$$

$$2NaAlSi_3O_8 + 2H^+ + H_2O = Al_2Si_2O_5(OH)_4 + 2Na^+ + 4SiO_2 \quad (2)$$

252 The CO_2 partial pressure pCO_2 was fixed during the course of the simulations to approximate the
253 buffering caused by an almost unlimited CO_2 source from the atmosphere. This specification
254 allows tracking the amount of CO_2 consumed by silicate weathering reactions assuming that the
255 reaction product HCO_3^- exiting the model domain is further transported to the sea, where it
256 precipitates as carbonates (Godderis et al., 2009) (Fig. 1).
257 A granitic mineral assemblage (quartz, potassium-feldspar, plagioclase, biotite) was assigned to
258 the solid part of the porous media to simulate typical continental silicate weathering processes.
259 Subsequently, the model was divided into a "fresh granite" domain and a domain that
260 experienced previous weathering (e.g., "altered granite") (Fig. 2), thus corresponding to the
261 saprolite zone of our conceptual model (Fig. 1). By varying the volume ratio between the "fresh
262 granite" and "altered granite" domain the effect of the proposed increasing exposure of the
263 silicate bedrock to chemical weathering on δ^7Li was assessed. By running the model for a
264 variable "fresh granite" contribution (i.e., varying volume ratio) we simulated the effect of a
265 varying chemical weathering intensity (i.e., varying saprolite thickness) on δ^7Li because a large
266 "fresh granite" or large "altered granite" contribution corresponds to a low or high weathering
267 intensity, respectively. Accordingly, we also assess earlier findings reporting that the chemical
268 silicate weathering intensity forms a first order control on aqueous δ^7Li (Huh et al., 2001;
269 Kisakürek et al., 2005; Pogge von Strandmann et al., 2006).
270 A mineralogical composition typical for the Sierra Nevada Batholith (Economos et al., 2010)
271 was defined for the "fresh granite" domain (Table 1). The initial mineralogical definition
272 included a bulk Li concentration of 24 ppm (Economos et al., 2010), which is similar to the
273 average upper-crustal Li concentration of 35±11 ppm (Teng et al., 2004). Owing to their similar
274 ionic radii, Li^+ substitutes easily for Mg^{2+} into the structural octahedral sites of silicate minerals

(Vigier et al., 2008). Furthermore, Li tends to accumulate in biotite (Kretz et al., 1989). Accordingly, Li was introduced into the model by specifying Li-bearing biotite using a Mg^{2+}-$_1Li^+{}_1K^+{}_1$ exchange (Table 2). Because in granitic environments, silicate mineral phases are predominantly weathered to kaolinite (Maher et al., 2009; Rudnick et al., 2004; White, 2002), and because goethite is the most widespread form of secondary iron oxides (Tardy and Nahon, 1985) Li-bearing kaolinite, and Li-bearing goethite were allowed to precipitate. By neglecting secondary Ca- and Mg-bearing minerals we do not fully investigate the fate of these two elements during silicate weathering. Our conceptual model (Fig. 1), however, assumes that riverine [Ca] and [Mg] are affected by carbonate weathering to ensure that carbonate precipitation and subsequent CO_2 consumption is occurring in the ocean, eventually.

TOUGHREACT V2 (Xu et al., 2011) computes mineral dissolution and precipitation reactions as kinetic reactions based on transition state theory (TST) (Lasaga, 1984)

$$r = A \cdot k \cdot \left(1 - \left(\frac{Q}{K}\right)^m\right)^n \qquad (3)$$

where A refers to the mineral reactive surface area ($m^2_{mineral}/kg_{H2O}$), k is the reaction rate constant ($mol/m^2/s$), Q refers to the ion activity product of a mineral dissolution/precipitation reaction (Table 2) and K is the corresponding equilibrium constant. Exponents m and n are fitting parameters that must be experimentally determined. For this study they were taken as equal to one, which is usually, but not always the case. In order to calculate effective precipitation and dissolution rates (eq. 3) reaction rate constants were defined according to Palandri and Kharaka (2004) whereas equilibrium constants were taken from the Soltherm.H06 database (Reed and

297 Palandri, 2006), which was derived using SUPCRT92 (Johnson et al., 1992). Mineral
298 stoichiometries, thermodynamic and kinetic parameters, and initial mineral and fluid
299 compositions are summarized in Tables 1 and 2.
300
301 *3.1.2. River simulations*
302 River simulations were conducted essentially as batch simulations, where the flow velocity was
303 set to zero (Fig. 2). In doing so, it was assumed that the reactive suspended load (i.e., solid
304 phase) is transported at the same velocity as river water, which is in agreement with current
305 knowledge about transport of suspended river loads (Fryirs and Brierley, 2013). Simulating
306 reactive transport in rivers by means of a batch simulation is justified because only the relative
307 transport velocity between aqueous and solid phase (i.e., suspended load) matters, whereas the
308 actual velocity of the two phases has no effect as long as aqueous and solid phases are
309 transported at the same velocity.
310 Two grid blocks of 1x1x1 m each were defined to simulate that subsurface waters exfiltrating
311 into river systems are diluted by river water, which previously experienced no or only minor
312 water-rock interaction. Consequently, steady-state concentrations obtained at the downstream
313 model boundary of the subsurface simulations were taken as input concentrations for one of the
314 two grid blocks, while pure water in equilibrium with CO_2 was defined as the initial
315 concentration for the second grid block (Fig. 2). It should be noted, that this particular grid block
316 has no geochemical meaning other than ensuring that exfiltrated subsurface water is diluted
317 during its transport in the river. Due to the initial concentration gradient, a diffusive flux J_{Di}
318 occurred between the two grid blocks, expressed as
319

$$J_{D_i} = \frac{\phi \cdot \tau \cdot D_{aq} \cdot A_{Interface}}{d_1 + d_2} \cdot \frac{dC_i}{dx} \quad (4)$$

where D_{aq} refers to the molecular diffusion coefficient of aqueous species (~10^{-9} m^2/s), $A_{Interface}$ (m^2) is the interfacial area between the two grid blocks, dC_i/dx ($mol/kg_{H2O}/m$) is the concentration gradient of species i, d_1 and d_2 (m) refer to the distances from the center of the two grid blocks to their mutual interface, and Φ and τ are the porosity and tortuosity, respectively. Reactions between the suspended river load and river waters were only considered for the grid block initially containing exfiltrating subsurface water. By setting the corresponding porosity to a very large value of 99.9% (Fig. 2), it was ensured that the suspended load only forms a minor fraction of the total river volume. The tortuosity was set to 1.0 for both grid blocks.

The same initial granitic mineralogical composition as for the subsurface "fresh granite" domain was assigned to the suspended river load (Table 2). In doing this, we assume that the suspended load contains a significant amount of primary silicate minerals in addition to the dominant clays and oxides (Gaillardet et al., 1999). This model assumption is consistent with Bouchez et al. (2011) who observed that the mineralogical composition of the suspended load is dependent on the particle size and that primary silicate minerals (e.g., quartz, albite) are enriched in the coarser fraction. Consequently, new goethite and kaolinite are allowed to precipitate and Li isotope fractionation in the simulated river thus occurs in the same fashion as in the subsurface simulations. As long as primary silicate minerals are exposed to chemical weathering, our river simulations are not sensitive to the ratio between primary and secondary minerals. Accordingly, we did not change the initial mineral volume fraction when compared to the subsurface simulations (Table 1).

3.2. Simulation of Li isotopic fractionation

To simulate Li isotopic fractionation, ^{6}Li and ^{7}Li were incorporated into the mineral stoichiometries of biotite, kaolinite and goethite (Table 2). An initial $\delta^{7}Li$ value of 0.0‰ was assumed for Li-bearing biotite corresponding to the average $\delta^{7}Li$ value of the upper continental crust (Teng et al., 2004). Assuming stoichiometric biotite dissolution, our simulations agree with previous studies showing that no or only minor Li isotopic fractionation occurs during mineral dissolution (Huh et al., 2004; Pistiner and Henderson, 2003). In contrast, our model considers Li isotopic fractionation during Li incorporation into precipitating kaolinite and goethite, using a solid solution approach similar to the one described for simulating Sr and Cr isotopic fractionation (Sonnenthal et al., 1998; Wanner and Sonnenthal, 2013). It should be noted, however, that Li must be treated slightly differently because it is incorporated into secondary minerals as a trace element, whereas Cr and Sr can be major constituents of minerals controlling the fate of Cr and Sr isotopes (e.g., $Cr(OH)_3$ and $SrCO_3$). Particularly challenging is the fact that, although some suggestions are found in the literature (Pistiner and Henderson, 2003; Vigier et al., 2008), it has not yet been shown how Li structurally substitutes into kaolinite and goethite. Because of this lack of detailed mineralogical knowledge, our model assumes a solid solution with three different endmembers (Fig. 3) to simulate Li uptake and associated Li isotopic fractionation during kaolinite and goethite precipitation: (i) a pure, non-Li bearing kaolinite and goethite endmember, (ii) a pure ^{6}Li bearing mineral endmember and (iii) a pure ^{7}Li bearing endmember. The pure ^{6}Li and ^{7}Li endmembers are hypothetical, but their specification allows fitting experimentally observed aqueous Li concentrations as well as measured amounts of Li that are incorporated in secondary minerals by calibrating the corresponding log(K) values.

The precipitation rate r_{prec} of the Li bearing kaolinite and goethite solid solution is defined as the sum of the individual endmember (Fig. 3) precipitation rates $r_{pure2nd}$, r_{6Li} and r_{7Li}:

$$r_{prec} = r_{pure2nd} + r_{^6Li} + r_{^7Li} \quad (5)$$

The rate of a specific endmember, r_{endm}, is calculated according to a TST-like expression

$$r_{endm} = A \cdot k \cdot \left(1 - \frac{Q_{endm}}{K_{endm}}\right) + k \cdot A \cdot \left(x_{endm} - 1\right) \quad (6)$$

where x_{endm} refers to the mole fraction of a specific secondary mineral endmember. For the hypothetical, pure ^{6}Li and ^{7}Li endmembers x_{6Li} and x_{7Li} are calculated according to:

$$x_{^6Li} = \frac{Q_{^6Li} / K_{^6Li}}{Q_{^6Li} / K_{^6Li} + Q_{^7Li} / K_{^7Li}} \quad (7)$$

$$x_{^7Li} = \frac{Q_{^7Li} / K_{^7Li}}{Q_{^6Li} / K_{^6Li} + Q_{^7Li} / K_{^7Li}} \quad (8)$$

Equations (7) and (8) ensure that the amount of Li that is incorporated into goethite and kaolinite reflects the Li concentration of the aqueous solution. Accordingly, the amount of Li removed by precipitation increases with increasing aqueous Li concentration. By doing so, our model is in good agreement with an experimental study showing that [Li] of synthesized smectites are linearly correlated with the corresponding aqueous [Li] (Decarreau et al., 2012).

385 Using the solid solution approach described above allows conveniently specifying a particular Li
386 isotopic fractionation factor α and corresponding enrichment factor ε for our simulations:
387
388 $$\alpha = \frac{K_{^6Li}}{K_{^7Li}} \quad (9)$$
389
390 $$\varepsilon = (\alpha - 1) \cdot 1000 \approx \Delta^7 Li = \delta^7 Li_{2ndMin} - \delta^7 Li_{solution} \quad (10)$$
391
392 Experimentally-determined Li isotopic enrichment factors for Li incorporation into precipitating
393 minerals ($\Delta^7Li_{2ndMin\text{-}solution} = \delta^7Li_{2ndMin} - \delta^7Li_{solution}$) have so far only been reported for smectite,
394 yielding values between -1.6 (at T=250°C) and -16.5‰ (at T=25°C), depending on the
395 experimental temperature (Vigier et al., 2008; personal communication). Other studies
396 determined Δ^7Li values between dissolved and suspended Li loads in rivers yielding $\Delta^7Li_{suspended\text{-}}$
397 $_{dissolved}$ from -6 to -36‰ (Huh et al., 2001; Kisakürek et al., 2005; Pogge von Strandmann et al.,
398 2010; 2006). Because of this relatively sparse dataset, we assigned a Li isotopic enrichment
399 factor of -20‰ for kaolinite as well as for goethite precipitation, which is within the range of Li
400 isotopic enrichment factors reported or inferred for secondary mineral precipitation.
401 Li adsorption on solid surfaces has been proposed as an additional process causing Li isotopic
402 fractionation (Pistiner and Henderson, 2003; Zhang et al., 1998). Significant fractionation (ε = -
403 13‰) was reported for an experiment involving Li adsorption via surface complexation reactions
404 at gibbsite surfaces (Pistiner and Henderson, 2003). Moreover, enrichment factors of -21‰ and -
405 29‰ were experimentally determined for Li adsorption on kaolinite and vermiculite,
406 respectively (Zhang et al., 1998). These enrichment factors, however, were determined by solely

studying the dissolved Li and no information regarding the surface complexation or substitution reaction is available. In contrast, very little Li isotopic fractionation was observed during Li exchange (i.e., ion exchange rection) with smectite interlayers (Pistiner and Henderson, 2003, Vigier et al., 2008). Overall, experimental data suggest that Li isotopic fractionation is caused by surface complexation reactions associated with a changing Li coordination chemistry or by Li substitution into crystal lattices. In contrast, physical Li adsorption by ion exchange reactions does not seem to cause significant fractionation. Similar to Bouchez et al. (2013) our model does not distinguish between Li exchange-, Li surface complexation-, or Li substitution reactions and Li uptake by secondary minerals and associated Li isotopic fractionation is solely simulated as a crystallographic substitution reaction during the formation of kaolinite and goethite such as discussed earlier.

Li isotope fractionation inherited from differences in the aqueous ^{6}Li and ^{7}Li diffusive flux was neglected because kaolinite and goethite precipitation was not assumed to be transport-limited by Li diffusion.

4. Model results and discussion

4.1. Simulation of the current weathering pattern (Fig. 1b)

To simulate the inferred current weathering pattern with predominant weathering of primary silicate minerals (Fig. 1) a "fresh granite" mineralogical composition was assigned to the entire subsurface model domain (i.e., 100% "fresh granite") and the pCO_2 was fixed to the approximate current atmospheric pCO_2 of ca. 370 ppm volume (ppmV) (Keeling, 1960). The solubility of the pure, but hypothetical Li-bearing kaolinite and goethite endmember (log(K)) was calibrated to -

2.6 (Table 2) to get a maximum kaolinite and goethite Li concentration within the subsurface domain of 200 ppm. A maximum value of 200 ppm is in agreement with Li concentration measurements in continental clays (Tardy et al., 1972). For the subsurface simulations, reactive surface areas for primary mineral phases were set to 1-2 cm^2/g (Table 2) to obtain a Li concentration at the end of the subsurface domain (4.08 μg/L, Fig. 4a,d) that is larger than the global average riverine value of 1.83 μg/L (Misra and Froelich, 2012). A reactive surface area of 1-2 cm^2/g also ensured that chemical equilibrium was not fully established within the subsurface domain and that primary mineral dissolution was occurring along the full domain (Fig. 4b,e). Reactive surface areas of precipitating kaolinite and goethite were set to the high value of 6824 cm^2/g based on Dobson et al. (2003).

With the specified parameters, our model yielded a continuous δ^7Li increase along the subsurface model domain reaching a dissolved δ^7Li value of roughly +10‰ at the downstream model boundary (Fig. 4a,d). It should be noted that the slope of the δ^7Li increase with residence time is dependent on the specified enrichment factor. For lower factors (i.e., less fractionation), longer residence time is needed to reach the same δ^7Li as for ε= -20‰, or vice versa. However, the correlation between δ^7Li and residence time is not sensitive to the specified enrichment factor. A δ^7Li value of +10‰ is significantly lower than the current global average riverine δ^7Li value of +23‰, (Misra and Froelich, 2012) implying that Li isotopic fractionation occurring in rivers form a major contribution on riverine δ^7Li. This simulation finding is supported by δ^7Li values derived from groundwaters and rivers draining the Columbia River basalt as well as small granitic catchments yielding significantly larger δ^7Li values for river samples (Lemarchand et al., 2010; Liu et al., 2014). Consequently, the reactive surface area of the suspended river load $A_{suspended\_load}$ was calibrated to 6000 cm^2/g (Table 2) for the corresponding river simulation to

match the global average riverine δ^7Li value (+23‰) after a simulated river residence time of 20 days, for which all river simulations were run (Fig. 4a). Similarly, the interfacial area between the two grid blocks of the river simulation $A_{interface}$ (eq. 4, Fig. 2) was set to 2560 m^2 to result in dilution of the exfiltrated groundwater by a factor of roughly 2. In doing so, the obtained Li concentration at the end of the river simulation (0.79, µg/L, Fig. 4a) was somewhat lower but still in the same order of magnitude as the global average riverine Li concentration of 1.83 µg/L (Misra and Froelich, 2012).

To explore the sensitivity of riverine δ^7Li on the reactivity of the suspended river load and thus on the actual suspended load concentration, the river simulation was performed for an $A_{suspended\_load}$ of 375 cm^2/g (Table 2). This value is 16 times lower than the initial surface area (6000 cm^2/g), and thus corresponds to the Misra and Froelich (2012) interpretation proposing that "the riverine Li flux has changed the ratio of dissolved to suspended partitioning from 4:1 in Paleocene to 1:4 today". Simulation results show that only minor Li isotopic fractionation takes place if the reactivity of the suspended load is this low (Fig. 4d). The high sensitivity of riverine δ^7Li on $A_{suspended\_load}$ implies that an increasing suspended river load concentration may have formed an important contribution on the seawater and global average riverine δ^7Li increase observed during the Cenozoic (Misra and Froelich, 2012).

Our simulation results also imply that riverine δ^7Li values increase with increasing subsurface residence time (Fig. 4a,d). This particular finding is in good agreement with seasonal riverine δ^7Li variations observed in streams draining the Columbia river basalt west of the Cascade Range, where seasonal precipitation and thus subsurface residence time variations are large (Liu et al., 2014). It is, however, unlikely that a Cenozoic global average subsurface residence time

475 increase caused the Cenozoic seawater δ^7Li increase because for an increasing relief (e.g., over
476 the Cenozoic), residence times tend to decrease and not to increase.
477
478 **4.2. Simulation of the Paleocene-Eocene boundary weathering pattern (Fig. 1a)**
479 A series of simulations with a varying "fresh granite" volume fraction corresponding to a varying
480 contribution of "fresh granite" weathering (i.e., varying weathering intensity) were run to match
481 riverine δ^7Li values inferred for the Paleocene-Eocene boundary. These simulations were run for
482 a fixed pCO_2 of 1200 ppmV to account for the atmospheric pCO_2 inferred for the Paleocene-
483 Eocene boundary (Li and Elderfield, 2013). For the "altered granite" domain the reactive surface
484 area of primary silicates was set to zero, thus simulating an extreme weathering intensity where
485 primary minerals are either fully replaced or fully coated by secondary minerals. Moreover, the
486 initial presence of Li-bearing kaolinite and goethite was specified for this model domain,
487 whereas their Li isotopic composition and initial volume fractions (e.g., δ^7Li = -10‰, Table 1)
488 were input from the results of a pure "fresh granite" run (i.e., 100% "fresh granite") after a
489 simulated time period of 100 years. In contrast to the runs simulating the current weathering
490 pattern, the varying weathering intensity runs were only performed for the subsurface domain
491 (Fig. 2) because our simulation results imply that only minor Li isotopic fractionation occurs
492 within rivers where the suspended river load concentration is low (Fig. 4d), which has been
493 inferred for the Paleocene-Eocene boundary (Misra and Froelich, 2012).
494 Model results show that downstream δ^7Li values become more positive with an increasing
495 contribution of "fresh granite" weathering (i.e., decreasing weathering intensity) (Fig. 5a). A
496 strong correlation between δ^7Li and fresh granite is, however, only observed for fresh granite
497 contributions <10%, which is inherited from the strong Li solubility contrast between the "fresh

498 granite" (i.e., Li-bearing biotite) and the "altered granite" domain (i.e., Li bearing kaolinite and
499 goethite) (Fig. 6). Nevertheless, our simulations imply that a decreasing weathering intensity
500 over the Cenozoic may have formed an important contribution to the Cenozoic seawater and
501 global average riverine δ^7Li increase (Misra and Froelich, 2012) in addition to the increasing
502 suspended river load concentration (Fig. 4a,d). Moreover, our simulations show that low global
503 average riverine δ^7Li values inferred for the Paleocene-Eocene boundary (Misra and Froelich,
504 2012) may have been inherited from predominant dissolution of previously formed secondary
505 mineral phases having a low δ^7Li value (e.g., -10‰, Fig. 6a) and a minor contribution of primary
506 silicate rock dissolution and corresponding precipitation of newly formed secondary mineral
507 phases associated with Li isotopic fractionation. For our simplified system (Fig. 2), a fresh
508 granite contribution of about 5% is required to obtain a δ^7Li value similar to the minimum value
509 inferred for the Paleocene-Eocene boundary at the downstream subsurface model boundary (e.g.,
510 +6‰, Fig. 5a). It should be noted that this particular interpretation is entirely different from the
511 one of Misra and Froelich (2012) because it does not rely on congruent weathering of primary
512 silicate minerals.
513
514 *4.2.1. Model uncertainty and mass balance considerations*
515 If a significant proportion of Li was adsorbed to goethite and kaolinite surfaces rather than fully
516 substituted into the crystal structure, Li solubility of weathering-intense, secondary mineral
517 dominated systems could be much higher than shown in Figure 6a. Especially for estuaries
518 where the ionic strength is higher than it is in aquifers or rivers, Li complexed to kaolinite and
519 goethite surfaces could be readily desorbed by surface complexation reactions involving other,

520 highly concentrated cations (e.g., Na, K, Ca, Mg). Such estuarine desorption has been shown for
521 various other trace metals (Du Laing et al., 2009).
522 Distinguishing between Li surface complexation and Li substitution reactions in our model
523 would simply change the slope and curvature of the δ^7Li vs. weathering intensity relation (Fig.
524 5a). Consequently, it would also change the amount of fresh granite weathering that is required
525 to obtain an inferred δ^7Li value of +6‰. The same applies if we were using a Li isotopic
526 enrichment factor other than -20‰, or if exchanged/complexed Li did not show the same δ^7Li
527 value than structural Li, which was observed for Mg (Wimpenny et al., 2014). However, our
528 main model observations, the overall inverse correlation between weathering intensity and
529 riverine δ^7Li would remain unchanged (Fig. 5a).
530 The above discussion illustrates that riverine [Li] derived from our model should be considered
531 as an end-member, minimum [Li] scenario for the Paleocene-Eocene boundary ([Li]=0.25 μg/L,
532 Fig. 5a). Updating the Misra and Froelich (2012) mass balance calculation with this [Li] as well
533 as the inferred minimum riverine δ^7Li (+6‰) yields seawater δ^7Li and [Li] of +24‰ and 112
534 μg/L, respectively. Whereas the calculated seawater δ^7Li is close to the observed value (+22‰,
535 Misra and Froelich, 2012), 112 μg/L is significantly lower than the inferred Paleocene-Eocene
536 seawater [Li] (179 μg/L), which is based on the assumption that seawater [Li] remained constant
537 throughout the Cenozoic (Misra and Froelich, 2012). If seawater [Li] was indeed constant, the
538 contradiction with the updated mass balance calculation could be resolved by increasing the
539 hydrothermal Li flux by a factor of about 1.6 or by increasing continental discharge by a factor
540 of ca. 7.3, both having only a minor effect on seawater δ^7Li (<1‰). However, only the
541 hydrothermal [Li] flux increase seems to be in a reasonable order of magnitude (Berner and
542 Kothavala, 2001; Otto-Bliesner, 1995).

When discussing mass balance calculations for the global Li cycle it should by noted that the calculations performed by Misra and Froelich (2012) are highly sensitive to Li isotopic fractionation occurring in the ocean during Li uptake by pelagic sediments and alteration of the basaltic oceanic crust (i.e., reverse weathering). For oceanic Li isotopic fractionation to cause a seawater δ^7Li shift less than +16‰, the Paleocene-Eocene boundary mass balance also works (i.e., seawater δ^7Li=+22‰) for riverine δ^7Li and/or [Li] (i.e., Li flux) larger than the ones derived from our end-member considerations ([Li]=0.25 μg/L, δ^7Li=+6‰, Fig. 5a).

In summary, a reasonable mass balance can be formulated with riverine [Li] and δ^7Li derived from our model ([Li]=0.25 μg/L, δ^7Li=+6‰, Fig. 5a). This suggests that for the Paleocene-Eocene boundary, riverine [Li] could have been significantly lower than it is today (Fig. 5a). However, it has to be appreciated that any mass balance calculation for past global Li cycles is affected by a relatively large uncertainty and it is beyond the scope of this study to provide accurate numbers for the one at the Paleocene-Eocene boundary. Without knowing the true global average riverine δ^7Li and [Li] for the Paleocene-Eocene boundary, our study can thus not rule out a (minor) contribution from a changing seawater hydrothermal Li flux and a changing magnitude of oceanic Li isotopic fractionation on the Cenozoic seawater δ^7Li increase.

5. Implications for using δ^7Li as a silicate weathering proxy

Previous studies did not show a distinct correlation between riverine δ^7Li and traditional silicate weathering proxies such as [Si], total cation charge TZ^+ ($TZ^+=Na^+ + K^+ + 2Mg^{2+} + 2Ca^{2+}$), normalized [Si] ($Si/TZ^+$), [Li], $^{87}Sr/^{86}Sr$, and Li/Na. (Huh et al., 2001; 1998; Millot et al., 2010; Pogge von Strandmann et al., 2010; 2006). For instance, Huh et al. (1998) did not observe a clear correlation between riverine δ^7Li and $^{87}Sr/^{86}Sr$, δ^7Li and [Li], as well as between δ^7Li and TZ^+,

566 whereas δ^7Li tended to be slightly negatively correlated with Si/TZ^+ when compiling available
567 global river data. Completing the Huh et al (1998) compilation with the numerous studies that
568 have emerged since the original publication displays an even more random distribution between
569 δ^7Li and TZ^+ (Fig. 7a), which was also observed for δ^7Li vs. [Li] (Misra and Froelich, 2012). In
570 contrast, the weak negative correlation between δ^7Li and Si/TZ^+ is still identified when updating
571 the global river compilation (Fig. 7b). For specific river systems, additional correlations were
572 observed. Examples include the strong inverse correlation between δ^7Li and $^{87}Sr/^{86}Sr$ as well as
573 between δ^7Li and Si/TZ^+ observed for the Orinoco drainage basin (Huh et al., 2001) and the
574 inverse correlation between δ^7Li and [Si] as well as between δ^7Li and [Li] observed in rivers
575 draining mostly basalt (Pogge von Strandmann et al., 2010; 2006). More recently, Millot et al.
576 (2010) and Liu et al. (2014) have shown that δ^7Li can display a negative correlation with Li/Na
577 that also might have global significance. In fact, a negative correlation between δ^7Li and Li/Na is
578 also identified in our updated global river compilation (Fig. 7c).
579 Plotting [Li], [Si] and TZ^+ along our model domain as well as against δ^7Li reveals that δ^7Li only
580 forms a distinct correlation with such concentration proxies for a particular system (subsurface
581 vs. river) (Figs. 4a,c and 5a-b). The transition from a positive correlation in the subsurface to a
582 negative one within rivers occurs because once exfiltrated into a river, aqueous species
583 concentrations decrease due to mixing with more diluted river water, while Li isotopic
584 fractionation is ongoing. We thus propose that the identified great importance of Li isotopic
585 fractionation occurring in rivers forms the main reason why concentration proxies do not show a
586 distinct correlation with global riverine δ^7Li values (e.g., δ^7Li vs. TZ^+, Fig. 7a; δ^7Li vs. [Li],
587 Misra and Froelich, 2012). If Li isotopic fractionation was only occurring in the subsurface we
588 would expect a positive correlation between δ^7Li and concentrations proxies such as TZ^+ (i.e.,

589 subsurface trend, Figs. 7a) because δ^7Li and TZ^+ (and any other concentration proxies) mainly
590 reflect the subsurface residence time (Figs. 4a-b) as well as the corresponding weathering
591 intensity (Fig. 5a-b). Instead, our simulations suggest that riverine δ^7Li values reflect a particular
592 combination of Li isotopic fractionation occurring within the subsurface as well as in rivers such
593 as illustrated with the corresponding trends (Fig. 7a).
594 Subsurface and riverine trends shown on Figure 7a are derived from simulating a mono
595 lithological subsurface that does not fully reach chemical equilibrium. Accordingly, the
596 simulation results should be considered as simplified trends only. The observation that in natural
597 aquifers δ^7Li and [Li] are not always positively correlated (Meredith et al., 2013; Négrel et al.,
598 2010; Tomascak et al., 2003) implies that additional parameters such as host rock mineralogy,
599 hydrodynamic mixing of various groundwater types and aquifer residence time distribution in
600 relation to chemical equilibrium (Maher, 2011) must be all taken into account to fully understand
601 the relation between δ^7Li and concentration proxies of a particular system (subsurface+river).
602 Moreover, we emphasize that the riverine trend on Figure 7a does not imply that δ^7Li is
603 increasing with distance along a river, which would be in contradiction to field observations
604 (Kisakürek et al., 2005; Pogge von Strandmann et al., 2006). For our river simulations a
605 correlation between δ^7Li and residence time (i.e., distance) is observed (Fig. 4a) because the ratio
606 between Li isotopic fractionation occurring in rivers vs. the one occurring in aquifers is
607 increasing with increasing river residence time. In other words, for natural rivers we only expect
608 increasing riverine δ^7Li with distance if the ratio of riverine Li isotopic fractionation vs.
609 subsurface fractionation is increasing with flow distance. This ratio, however, is only changing if
610 the subsurface residence time distribution is changing along a river.

611 Our simulation results agree well with the globally observed negative correlations between δ^7Li
612 and Li/TZ$^+$ and between δ^7Li and Li/Na (Fig. 7b-c) because the parameters that increase δ^7Li
613 (residence time increase, suspended river load concentration increase, weathering intensity
614 decrease) cause a decrease in the simulated Si/TZ$^+$ and Li/Na ratio (Figs. 4c and 5b). For a
615 silicate setting also affected by newly formed secondary Ca- and Mg-bearing phases, we would
616 expect a similar behavior for Ca/TZ$^+$ and Mg/TZ$^+$ as well as for Ca/Na and Mg/Na. The
617 simulated negative correlation between δ^7Li and Si/TZ$^+$ as well as between δ^7Li and Li/Na (Figs.
618 4a and 5b) is mainly observed because the δ^7Li increase is inherited from an increasing amount
619 of Li being incorporated in kaolinite and goethite with increasing aqueous [Li], whereas Na
620 remains in solution. Precipitation of Li-bearing kaolinite also removes Si from the aqueous
621 solution, which explains why Si/TZ$^+$ is decreasing with increasing Si concentration (Fig. 4a-b
622 and 5b). The Si/TZ$^+$ decrease is most prominent if [Si] approaches a solubility controlled
623 maximum such as observed towards the end of our subsurface domain (i.e., t>100d, Fig. 4a-b).
624 In fact, the low sensitivity of δ^7Li on Si/TZ$^+$ for short subsurface residence times (Fig. 4b) is
625 likely the reason why the negative correlation between δ^7Li and Si/TZ$^+$ is less pronounced than
626 the one between δ^7Li and Li/Na in global rivers (Fig. 7b-c).
627
628 **5.1. Seawater δ^7Li*: a proxy for Cenozoic continental silicate weathering rates?**
629 We propose that Si/TZ$^+$ as well as Li/Na are only particular and thus somewhat arbitrary proxies
630 that correlate with δ^7Li (Figs. 7b-c). Most importantly, it has not been shown yet how these
631 ratios could serve as quantitative proxies for silicate weathering rates. We therefore postulate that
632 the extent of water-rock interaction occurring along a particular flow path (subsurface + river)
633 forms a more fundamental parameter that defines a system's δ^7Li. In fact, our simulation results

(Figs. 4c and 5b) clearly show that the amount of primary silicate mineral dissolution (quartz, feldspars, biotite) is positively correlated with δ^7Li. The correlation occurs because the amount of mineral dissolution reflects an aquifer's residence time, the suspended river load concentration, and the weathering intensity, which have been identified to form the major controls on riverine δ^7Li (Figs. 4c and 5b). Our simulations thus imply that aqueous δ^7Li is highly correlated with the total amount of water-rock interaction occurring along a particular flow path (in moles) suggesting that δ^7Li is almost a perfect silicate weathering tracer. The positive correlation between δ^7Li and silicate mineral dissolution (Figs. 4c and 5b), however, does not necessarily imply a correlation between δ^7Li and silicate weathering rates (in moles/year). To obtain such weathering rates for a particular flow path, amounts of primary silicate mineral dissolution have to be multiplied by subsurface and riverine discharges. Subsurface and riverine discharges are closely related to the corresponding residence times. Accordingly, the previously identified lack of sensitivity of Cenozoic residence time variations on the Cenozoic seawater δ^7Li record implies that this particular δ^7Li record is not sensitive to discharge variations either. This finding is supported by Otto-Bliesner (1995) reporting that continental runoff remained roughly constant over the Cenozoic (±10%).

Assuming minor effects from discharge variations, the simulated positive correlation between primary silicate mineral dissolution and riverine δ^7Li (Figs. 4c and 5b) suggests that the Cenozoic seawater δ^7Li increase (Misra and Froelich, 2012) was most likely caused by globally increasing continental silicate weathering rates. This finding strongly supports the Misra and Froelich (2012) hypothesis arguing that the Cenozoic seawater δ^7Li increase is inherited from increasing riverine δ^7Li values as a result of major Cenozoic tectonic uplift (e.g., Himalayan orogeny). The main argument for this statement is that uplift has a first order control on both

parameters identified to increase silicate weathering rates as well as riverine δ^7Li values (weathering intensity and suspended river load concentration, Figs. 4c and 5a). This agreement is notable because our understanding of Li isotope fractionation processes does not rely on congruent weathering and is thus entirely different from the one of Misra and Froelich (2012).

In contrast to tectonic uplift, Cenozoic cooling occurring since the humid PETM (Clementz and Sewall, 2011; Miller et al., 1987) does not seem to have a distinct effect on δ^7Li. Whereas Cenozoic cooling may have contributed to the Cenozoic weathering intensity decrease and corresponding δ^7Li increase, cooling reduces the amount of primary silicate mineral dissolution along a specific flow path and drives δ^7Li to lower values (Fig. 4c). δ^7Li measurements from streams draining the Columbia River basalt under significantly different climatic conditions (dry vs. wet) confirm that climate does not necessarily have a first order control on riverine δ^7Li (Liu et al., 2014).

6. Implications for CO_2 consumption by silicate weathering

The identified positive correlation between δ^7Li and the amount of primary silicate mineral dissolution (Figs. 4c and 5b) suggests that, over the last 56 Ma, riverine δ^7Li was closely correlated to the amount of CO_2 consumed by silicate weathering reactions (Table 2) assuming that carbonic acid (H_2O+CO_2, eq. 1) forms the major proton source for these reactions and that continental discharge remained roughly constant (Otto-Bliesner, 1995). Accordingly, the Cenozoic seawater δ^7Li record and the derived global average riverine δ^7Li record provide a potential opportunity to quantify the amount of CO_2 that was consumed by silicate weathering reactions throughout the Cenozoic.

In particular, reactive transport modeling such as performed here allows explicitly quantifying the amount of CO_2 that was consumed along a specific flow path by integrating the amount of each mineral $N_{Mineral}$ (mole) that was dissolved along the full model domain during a specific simulation period:

$$N_{CO_2} = 4 \cdot \sum N_{albite} + 4 \cdot \sum N_{anorthite} + 4 \cdot \sum N_{Kspar} + 10 \cdot \sum N_{biotite} + 0 \cdot \sum N_{quartz} - 6 \cdot \sum N_{kaolinite} - 2 \cdot \sum N_{goethite} \quad (11)$$

The dissolved mineral amounts ($N_{Mineral}$) are scaled by the amount of H^+ that is required to dissolve one mole of a specific mineral phases (e.g., 4 for albite, Table 2) because one mole of H^+ is added to the solution (i.e., CO_2 is consumed by mineral dissolution) if one mole of atmospheric CO_2 is dissolved (eq. 1). The amount of kaolinite precipitation times 6 and the amount of goethite precipitation times 2, respectively (i.e., stoichiometric coefficient of H^+, Table 2) were subtracted because kaolinite and goethite precipitation adds H^+ to the system and liberates the same mole amount of CO_2 to keep the pCO_2 at the specified fixed value (i.e., CO_2 is liberated by kaolinite and goethite precipitation). Equation (11) assumes that dissolved HCO_3^- precipitates as carbonates in the ocean (Fig. 1) such as shown here for calcite ($CaCO_3$) precipitation:

$$Ca^{2+} + HCO_3^- = CaCO_3 + H^+ \quad (12)$$

Applying equation (11) to our simulation runs indeed yields a positive correlation between δ^7Li and CO_2 consumption (Figs. 4c and 5b) implying that CO_2 consumption by continental silicate

weathering increased over the Cenozoic. This finding agrees well with the carbon cycle model of Li and Elderfield (2013) also suggesting an increase in continental silicate weathering and corresponding CO_2 consumption rates over the Cenozoic. However, our modeling approach relies on thermodynamic parameters for Li-bearing minerals that are only roughly constrained so far (e.g., fractionation factor, crystallographic substitution reaction, Li concentration of secondary minerals, Li solubility). Accordingly, our modeling approach should only be applied to qualitatively identify geochemical trends related to Li isotopic fractionation such as performed here. Once these thermodynamic parameters have been determined, a reliable quantification of the amount of CO_2 consumed by silicate weathering over the Cenozoic would require incorporating basalt weathering in addition to granite weathering, because basalt weathering accounts for more than 30% of global CO_2 consumption by silicate weathering even though basalts only form about 8% of exposed silicate rocks today (Gaillardet et al., 1999).

Our CO_2 consumption calculations also show that the amount of CO_2 consumed by pure "fresh granite" weathering (e.g., 100% contribution) was the same for the current and the Paleocene-Eocene weathering pattern simulations (17 kmol, Figs. 4b and 5b). The same applies for the simulated δ^7Li values at the downstream subsurface model boundary (+10‰). This observation emphasizes that CO_2 consumption by continental silicate weathering reactions is more sensitive to specific primary silicate mineral phases that are exposed to chemical weathering rather than to atmospheric pCO_2. Moreover, it suggests that pCO_2 variations during the Cenozoic (Li and Elderfield, 2013) do not seem to have a distinct control on the Cenozoic seawater δ^7Li record.

To extend the use of seawater δ^7Li values to reconstruct CO_2 consumption by continental silicate weathering for geological times other than the past 56 Ma, potential significant changes in continental river discharge have to be taken into account as well. Whereas discharge variations

seem less important for the Cenozoic, a dramatic acceleration of the hydrological cycle caused by a short term atmospheric pCO_2 increase shifted seawater δ^7Li values by about -10‰ within a short period of time (100 ky) during Cretaceous Oceanic Anoxic Event 2 (OAE2) (Pogge von Strandmann et al., 2013). Because an accelerated hydrological cycle likely shifted discharge to higher values and residence times to lower values, the low OAE2 δ^7Li values correspond well with our simulated positive correlation between residence time and δ^7Li (Fig. 4a). Interestingly, the negative δ^7Li excursion observed for OAE2 was attributed to enhanced continental silicate weathering forming a negative feedback on the inferred pCO_2 increase (Pogge von Strandmann et al., 2013). This finding is opposite to the one made for the Cenozoic because for the past 56 Ma, inferred increasing silicate weathering rates are manifested by a δ^7Li increase (Misra and Froelich, 2012; this study) while for OAE2 they are accompanied by a δ^7Li decrease (Pogge von Strandmann et al., 2013). This apparent contradiction is, however, well explained by our modeling results revealing that seawater and inferred riverine δ^7Li values are simply a function of the amount of silicate weathering and corresponding CO_2 consumption along a specific flow path (in moles) (Figs. 4c and 5b). However, they are not necessarily correlated with silicate weathering and CO_2 consumption rates (in moles/year) on which discharge has a first order control (Gaillardet et al., 1999). The opposing behavior of δ^7Li with increasing silicate weathering rates thus highlights the importance of reconstructing past discharge rates, which, owing to the strong correlation between silicate weathering rates and discharge (Gaillardet et al., 1999), is indispensable for quantifying past CO_2 consumption rates based on seawater δ^7Li measurements.

7. Summary and conclusions

A novel reactive transport modeling approach was developed to simulate Li isotopic fractionation during Li uptake by secondary mineral phases. Simulation results show that riverine δ^7Li is controlled not only by the Li isotopic fractionation factor but also by the subsurface residence time of infiltrating meteoric water, the corresponding weathering intensity and the concentration of a river's suspended load.

Based on these identified factors, we presented a new interpretation of the previously reported Cenozoic seawater δ^7Li record (Misra and Froelich, 2012) that does not rely on geochemically unlikely congruent weathering. In particular, modeling results imply that the low seawater δ^7Li observed at the Paleocene-Eocene boundary could be inherited from a high weathering intensity with predominant weathering of previously-formed secondary mineral phases (e.g., clays, oxides, hydroxides) having a low δ^7Li and a low contribution of incongruent silicate mineral dissolution with associated secondary mineral formation and Li isotopic fractionation. Moreover, simulation results imply that the Cenozoic seawater δ^7Li increase was likely caused by an increasing amount of primary silicate mineral dissolution (i.e., decreasing weathering intensity, increasing suspended river load concentration) inherited from tectonic uplift and a corresponding global relief increase. In contrast, Cenozoic cooling and corresponding pCO_2 and precipitation variations do not seem to have a distinct control on the Cenozoic seawater δ^7Li record. It is thus emphasized that our modeling results strongly favor the original Raymo and Ruddiman (1992) model stating that a tectonically-driven increase in silicate weathering rates may have caused the inferred Cenozoic atmospheric pCO_2 decrease. However, another Li isotope study has shown that for dramatic, short term events increasing atmospheric pCO_2 and triggering warmer temperatures (e.g., Cretaceous OAE2), silicate weathering and corresponding CO_2 consumption rates can be dramatically increased without major tectonic uplift (Pogge von Strandmann et al., 2013).

771 The identified strong correlation between Cenozoic silicate weathering rates and δ^7Li implies
772 that seawater and global average riverine δ^7Li values are closely related to global CO_2
773 consumption by continental silicate weathering. For an actual quantitative correlation, however,
774 more experimental and modeling work is required. Key parameters are the temperature-
775 dependent thermodynamic properties of specific Li bearing primary and secondary minerals
776 (e.g., crystallographic Li substitution and surface complexation reactions, maximum Li
777 substitution, Li solubility, Li isotope fractionation factor) as well as the determination of global
778 average continental discharge through time.
779 Incorporating Li isotopic fractionation into reactive transport model simulations of subsurface
780 and river systems also improved the understanding of the δ^7Li distribution observed in global
781 rivers today. Simulation results revealed that Li isotope fractionation occurs in the subsurface as
782 well as in river systems. Fractionation occurring in both systems seems to be the main reason
783 why no or only weak correlations between global riverine δ^7Li values and traditional silicate
784 weathering proxies such as [Si], [Li], Si/TZ^+ are observed. The lack of correlation is observed
785 because once exfiltrated into rivers, elemental concentrations are diluted by a larger flux of
786 superficial river waters while Li isotopic fractionation is still ongoing.
787 Finally, this study illustrates that reactive transport modeling is a powerful tool for a (semi)-
788 quantitative interpretation of stable isotope ratios. In comparison to closed system Rayleigh-type
789 or steady state flux models, it bears the advantage of considering the full thermodynamic
790 properties of involved mineral phases (e.g., mineral stoichiometry, mineral solubility, kinetic
791 dissolution/precipitation) as well as assessing the effect of transport on isotopic fractionation.
792 The presented solid solution approach can be easily applied to other isotopic systems (e.g., Si,

Mg, Ca, Mo), which have also been shown to serve as potentially powerful weathering proxies (Moore et al., 2013; Tipper et al., 2012; Voegelin et al., 2012; Ziegler et al., 2005).

ACKNOWLEDGMENTS

This work was supported by the U.S. Department of Energy, Geothermal Technologies Program, Energy Efficiency and Renewable Energy Office, Award No GT-480010-12. Postdoctoral fellowship support was provided to X-ML by the Carnegie Institution of Washington. The manuscript significantly benefited from a helpful editorial handling by Michael Böttcher, and very constructive comments by Philip Pogge von Strandmann and an additional, anonymous reviewer.

Figure and table captions

Fig. 1

Proposed weathering and Li isotopic fractionation model for the Paleocene-Eocene boundary (a) and for today (b) in terms of idealized crustal cross sections along a major river system. Black arrows show typical flow paths for meteoric water infiltrating into the subsurface and being transported in groundwater systems before exfiltrating into a major river system. Increasing Cenozoic seawater δ^7Li values (Misra and Froelich, 2012) are explained by an increasing availability of bedrock (primary) silicates for chemical weathering (i.e., decreasing weathering intensity, increasing suspended river load) as the global relief increases and the average saprolite thickness becomes smaller. For the current weathering pattern, chemical weathering of primary silicates and subsequent precipitation of secondary minerals (clays, Fe- and Al-hydroxides)

fractionate Li isotopes by accumulating ^{7}Li in the groundwater and ^{6}Li in the precipitating mineral phases. If only secondary silicate minerals are exposed to chemical weathering such as inferred for the Paleocene-Eocene boundary (a) no significant Li isotopic fractionation occurs. An increasing relief yields decreasing subsurface residence times as well as increasing suspended river load concentrations, both potentially affecting riverine $\delta^{7}Li$ in addition to the decreasing weathering intensity.

Fig. 2:

Model setup for simulating reactive transport in the subsurface and within rivers. Subsurface simulations were run for meteoric water infiltrated and transported along a 200 m long flow path eventually exfiltrating into a river system (e.g., arrows on Fig. 1). They were run for various fresh-to-altered granite volume fractions to simulate the effects of a varying silicate weathering intensity on $\delta^{7}Li$. Fluids flowing along the two model domains were fully mixed in the downstream model boundary ("mixing") to track the integrated Li isotopic signal. River simulations were run as batch simulations (no flow) assuming that the suspended load is transported at the same velocity as river water. Moreover, river simulations consider a diffusive dilution of the exfiltrated groundwater with water that experienced no previous water-rock interaction (i.e., pure water+CO_2). For both systems (subsurface and river), Li isotopic fractionation is simulated to occur during kaolinite and goethite precipitation.

Fig. 3:

Schematic illustration of the composition of modeled Li bearing secondary minerals, which were simulated as ideal solid solutions. The three endmembers were defined as pure goethite or

kaolinite with known thermodynamic properties, and hypothetical, but pure ^{6}Li and pure ^{7}Li, for which log(K) values have to be calibrated by matching observed secondary mineral and aqueous Li concentrations.

Fig. 4:

Model results for the simulated current weathering pattern with 100% "fresh granite" contribution (Fig. 1b). (a) and (d) illustrate steady state [Li] and [Si] along the full model domain (subsurface + river), as well as corresponding $\delta^{7}Li$ profiles ($\delta^{7}Li_{dissolved}$ and $\delta^{7}Li_{kaolinite}=\delta^{7}Li_{goethite}=\delta^{7}Li_{solids}$) for a reactive suspended river load surface area of 6000 cm^2/g and 375 cm^2/g, respectively, illustrating that the simulated $\Delta^{7}Li_{solids\text{-}dissolved}$ was equal to the initially specified Li isotope enrichment factor of ε=-20‰. (b) and (e) present corresponding steady state profiles of typical silicate weathering tracers such as TZ^{+} (in meqv/kg), Si/TZ^{+}, Li/TZ^{+} and Li/Na (molar ratio). Also shown are the cumulative primary mineral dissolution (quartz + feldspars + biotite) and corresponding CO_2 consumption (eq. (11)) profiles (in kmol) during a simulated time period of 100 years. c) and (f) illustrates the relationship between the parameters shown in (b) and (e) as a function of $\delta^{7}Li_{dissolved}$. Note that profiles except the ones shown in (c) and (f) are plotted against fluid residence time to simultaneously illustrate subsurface and river simulations. Along the subsurface domain (gray shaded area) fluid residence time (x-axis) corresponds also to the distance along the subsurface domain because the flow velocity was 1 m/d.

Fig. 5:

Model results for the simulated Paleocene-Eocene boundary weathering pattern (Fig. 1a). (a) Steady state [Si], [Li] and δ^7Li at the downstream subsurface model boundary ("mixing", Fig. 2) plotted as a function of the simulated "fresh granite" contribution or inverse weathering intensity, respectively. The dashed line illustrates that 5% fresh granite contribution is required to get an assumed Paleocene-Eocene boundary riverine δ^7Li value of +6‰, which in turn yields a corresponding [Li] of 0.25 µg/L. (b) Cumulative amounts of primary mineral dissolution (feldspars, biotite, quartz) and CO_2 consumption (in kmol) within the entire subsurface model domain during a simulated time period of 100 years as a function of steady state δ^7Li values at the downstream subsurface model boundary. Also shown are steady state TZ^+ (in meqv/kg), Si/TZ^+ and Li/Na (molar ratio) at the downstream subsurface model boundary as a function of corresponding δ^7Li values.

Fig. 6:

Simulated steady-state [Li] and δ^7Li profiles along the altered (a) and fresh granite domain (b) of the Paleocene-Eocene boundary weathering pattern (Fig. 1a).

Fig. 7:

Compilation of previously published riverine δ^7Li (Huh et al., 2001; 1998; Millot et al., 2010; Pogge von Strandmann et al., 2010; 2006; Vigier et al., 2009; Wimpenny et al., 2010b) plotted against various weathering tracers. (a) δ^7Li vs. TZ^+ ($TZ^+=[Na^+]+[K^+]+2[Ca^{2+}]+2[Mg^{2+}]$) and corresponding subsurface and riverine trend identified from simulation results (Fig. 4). (b) δ^7Li vs. Si/TZ^+. (c) δ^7Li vs. Li/Na. Samples affected by hydrothermal springs are not shown.

884 Table 1

885 Initial and boundary conditions

886

887 Table 2:

888 Simulated silicate weathering reactions

889

890 **REFERENCES**

891 Berner, R. A., Lasaga, A. C., Garrels, R. M., 1983. The carbonate-silicate geochemical cycle and
892 its effect on atmospheric carbon-dioxide over the past 100 million years. Am. J. Sci. 283,
893 641-683.
894 Berner, R. A., 1994. 3GEOCARB II: a revised model of atmospheric CO_2 over phanerozoic
895 time. Am. J. Sci. 294, 56-91.
896 Berner, R. A., Kothavala, Z., 2001. GEOCARB III: A Revised Model of Atmospheric CO_2 over
897 Phanerozoic Time. Am. J. Sci. 301, 182-204.
898 Bouchez, J., Gaillardet, J., France-Lanord, C., Maurice, L., Dutra-Maia, P., 2011. Grain size
899 control of river suspended sediment geochemistry: Clues from Amazon River depth
900 profiles. Geochemistry, Geophysics, Geosystems 12, Q03008.
901 Bouchez, J., Von Blanckenburg, F., Schuessler, J. A., 2013. Modeling novel stable isotope ratios
902 in the weathering zone. Am. J. Sci. 313, 267-308.
903 Clementz, M. T., Sewall, J. O., 2011. Latitudinal Gradients in Greenhouse Seawater $\delta^{18}O$:
904 Evidence from Eocene Sirenian Tooth Enamel. Science 332, 455-458.
905 Decarreau, A., Vigier, N., Pálková, H., Petit, S., Vieillard, P., Fontaine, C., 2012. Partitioning of
906 lithium between smectite and solution: An experimental approach. Geochim.
907 Cosmochim. Acta 85, 314-325.
908 Dobson, P. F., Kneafsey, T. J., Sonnenthal, E. L., Spycher, N., Apps, J. A., 2003. Experimental
909 and numerical simulation of dissolution and precipitation: implications for fracture
910 sealing at Yucca Mountain, Nevada. J. Cotam. Hydrol. 62-63, 459-476.
911 Du Laing, G., Rinklebe, J., Vandecasteele, B., Meers, E., Tack, F. M. G., 2009. Trace metal
912 behaviour in estuarine and riverine floodplain soils and sediments: A review. Sci. Total
913 Environ. 407, 3972-3985.
914 Economos, R. C., Memeti, V., Paterson, S. R., Miller, J. S., Erdmann, S., Zak, J., 2010. Causes
915 of compositional diversity in a lobe of the Half Dome granodiorite, Tuolumne Batholith,
916 Central Sierra Nevada, California. Earth Env. Sci. T. R. So. 100, 173-183.
917 Edmond, J. M., Palmer, M. R., Measures, C. I., Grant, B., Stallard, R. F., 1995. The fluvial
918 geochemistry and denudation rate of the Guayana Shield in Venezuela, Colombia, and
919 Brazil. Geochim. Cosmochim. Acta 59, 3301-3325.
920 Francois, L. M., Godderis, Y., 1998. Isotopic constraints on the Cenozoic evolution of the carbon
921 cycle. Chem. Geol. 145, 177-212.

Fryirs, K. A., Brierley, G. J., 2013. Geomorphic analysis of river Systems: an approach to reading the landscape. John Wiley & Sons.
Gaillardet, J., Dupré, B., Louvat, P., Allègre, C. J., 1999. Global silicate weathering and CO_2 consumption rates deduced from the chemistry of large rivers. Chem. Geol. 159, 3-30.
Godderis, Y., Roelandt, C., Schott, J., Pierret, M., Francois, L. M., 2009. Towards an integrated model of weathering, climate, and biosphere processes, in: Oelkers, E. H. and Schott, J. (Eds.), Towards an integrated model of weathering, climate, and biosphere processes. Mineralogical Society of America. Rev. Mineral. 70, 411-434.
Hathorne, E. C., James, R. H., 2006. Temporal record of lithium in seawater: A tracer for silicate weathering? Earth Planet. Sci. Lett. 246, 393-406.
Huh, Y., Chan, L. H., Zhang, L., Edmond, J. M., 1998. Lithium and its isotopes in major world rivers: Implications for weathering and the oceanic budget. Geochim. Cosmochim. Acta 62, 2039-2051.
Huh, Y., Chan, L. H., Edmond, J. M., 2001. Lithium isotopes as a probe of weathering processes: Orinoco River. Earth Planet. Sci. Lett. 194, 189-199.
Huh, Y., Chan, L. H., Chadwick, O. A., 2004. Behavior of lithium and its isotopes during weathering of Hawaiian basalt. Geochem. Geophy. Geosy. 5, Q09002.
Johnson, J. W., Oelkers, E. H., Helgeson, H. C., 1992. SUPCRT92: a software package for calculating the standard molal thermodynamic poroperties of minerals, gases, aqueous species, and reactions from 1 to 5000 bar and 0 to 1000 °C. Comput. Geosci. 18, 899-948.
Keeling, C. D., 1960. The concentration and isotopic abundances of carbon dioxide in the atmosphere. Tellus 12, 200-203.
Kisakürek, B., Widdowson, M., James, R. H., 2004. Behaviour of Li isotopes during continental weathering: the Bidar laterite profile, India. Chem. Geol. 212, 27-44.
Kisakürek, B., James, R. H., Harris, N. B. W., 2005. Li and δ7Li in Himalayan rivers: Proxies for silicate weathering? Earth Planet. Sci. Lett. 237, 387-401.
Kretz, R., Loop, J., Hartree, R., 1989. Petrology and Li-Be-B geochemistry of muscovite-biotite granite and associated pegmatite near Yelloknife, Canada. Contrib. Mineral. Petr. 102, 174-190.
Lasaga, A. C., 1984. Chemical kinetics of water-rock interactions. J. Geoph. Res. 89, 4009-4025.
Lemarchand, E., Chabaux, F., Vigier, N., Millot, R., Pierret, M.-C., 2010. Lithium isotope systematics in a forested granitic catchment (Strengbach, Vosges Mountains, France). Geochim. Cosmochim. Acta 74, 4612-4628.
Li, G., Elderfield, H., 2013. Evolution of carbon cycle over the past 100 million years. Geochim. Cosmochim. Acta 103, 11-25.
Li, G., West, A. J., 2014. Increased continental weathering flux through the Cenozoic inferred from the lithium isotope evolution of seawater. Earth Planet. Sci. Lett. in revison.
Liu, X.-M., Rudnick, R. L., McDonough, W. F., Cummings, M. L., 2013. Influence of chemical weathering on the composition of the continental crust: Insights from Li and Nd isotopes in bauxite profiles developed on Columbia River Basalts. Geochim. Cosmochim. Acta 115, 73-91.
Liu, X.-M., Wanner, C., Rudnick, R. L., McDonough, W. F., 2014. Novel interpretation of large Li isotopic variations produced by streams and ground waters draining basalts. Earth Planet. Sci. Lett. in review.

967 Maher, K., Steefel, C. I., White, A. F., Stonestrom, D. A., 2009. The role of reaction affinity and
968 secondary minerals in regulating chemical weathering rates at the Santa Cruz Soil
969 Chronosequence, California. Geochim. Cosmochim. Acta 73, 2804-2831.
970 Maher, K., 2011. The role of fluid residence time and topographic scales in determining
971 chemical fluxes from landscapes. Earth Planet. Sci. Lett. 312, 48-58.
972 Meredith, K., Moriguti, T., Tomascak, P., Hollins, S., Nakamura, E., 2013. The lithium, boron
973 and strontium isotopic systematics of groundwaters from an arid aquifer system:
974 Implications for recharge and weathering processes. Geochim. Cosmochim. Acta 112,
975 20-31.
976 Miller, K. G., Fairbanks, R. G., Mountain, G. S., 1987. Tertiary oxygen isotope synthesis, sea
977 level history, and continental margin erosion. Paleoceanography 2, 1-19.
978 Milliman, J. D., Meade, R. H., 1983. World-wide delivery of river sediment to the oceans. J.
979 Geol. 91, 1-21.
980 Millot, R., Vigier, N., Gaillardet, J., 2010. Behaviour of lithium and its isotopes during
981 weathering in the Mackenzie Basin, Canada. Geochim. Cosmochim. Acta 74, 3897-3912.
982 Misra, S., Froelich, P. N., 2012. Lithium isotope history of Cenozoic seawater: changes in
983 silicate weathering and reverse weathering. Science 335, 818-823.
984 Moore, J., Jacobson, A. D., Holmden, C., Craw, D., 2013. Tracking the relationship between
985 mountain uplift, silicate weathering, and long-term CO_2 consumption with Ca isotopes:
986 Southern Alps, New Zealand. Chem. Geol. 341, 110-127.
987 Müller, R. D., Sdrolias, M., Gaina, C., Steinberger, B., Heine, C., 2008. Long-term sea-level
988 fluctuations driven by ocean basin dynamics. Science 319, 1357-1362.
989 Négrel, P., Millot, R., Brenot, A., Bertin, C., 2010. Lithium isotopes as tracers of groundwater
990 circulation in a peat land. Chem. Geol. 276, 119-127.
991 Nesbitt, H. W., Young, G. M., 1982. Early Proterozoic climates and plate motions inferred from
992 major element chemistry of lutites. Nature 299, 715-717.
993 Oliver, L., Harris, N., Bickle, M., Chapman, H., Dise, N., Horstwood, M., 2003. Silicate
994 weathering rates decoupled from the $^{87}Sr/^{86}Sr$ ratio of the dissolved load during
995 Himalayan erosion. Chem. Geol. 201, 119-139.
996 Otto-Bliesner, B. L., 1995. Continental drift, runoff, and weathering feedbacks: Implications
997 from climate model experiments. J. Geophys. Res-Atmos. 100, 11537-11548.
998 Palandri, J. L., Kharaka, Y. K., 2004. A compilation of rate parameters of water-mineral
999 interaction kinetics for application to geochemical modeling. US Geological Survey.
1000 Report 2004-1068.
1001 Pistiner, J. S., Henderson, G. M., 2003. Lithium-isotope fractionation during continental
1002 weathering processes. Earth Planet. Sci. Lett. 214, 327-339.
1003 Pogge von Strandmann, P. A. E., Burton, K. W., James, R. H., van Calsteren, P., Gíslason, S. R.,
1004 Mokadem, F., 2006. Riverine behaviour of uranium and lithium isotopes in an actively
1005 glaciated basaltic terrain. Earth Planet. Sci. Lett. 251, 134-147.
1006 Pogge von Strandmann, P. A. E., Burton, K. W., James, R. H., van Calsteren, P., Gislason, S. R.,
1007 2010. Assessing the role of climate on uranium and lithium isotope behaviour in rivers
1008 draining a basaltic terrain. Chem. Geol. 270, 227-239.
1009 Pogge von Strandmann, P. A. E., Jenkyns, H. C., Woodfine, R. G., 2013. Lithium isotope
1010 evidence for enhanced weathering during Oceanic Anoxic Event 2. Nat. Geosci. 6, 668-
1011 672.

1012 Raymo, M. E., Ruddiman, W. F., 1992. Tectonic forcing of late Cenozoic climate. Nature 359,
1013 117-122.
1014 Reed, M., Palandri, J. L., 2006. SOLTHERM.H06, a database of equilibrium constants for
1015 minerals and aqueous species. Available from the authors, University of Oregon, Eugene,
1016 Or.
1017 Rowley, D. B., 2002. Rate of plate creation and destruction: 180 Ma to present. Geol. Soc. Am.
1018 Bull. 114, 927-933.
1019 Rudnick, R. L., Tomascak, P. B., Njo, H. B., Gardner, L. R., 2004. Extreme lithium isotopic
1020 fractionation during continental weathering revealed in saprolites from South Carolina.
1021 Chem. Geol. 212, 45-57.
1022 Singleton, M. J., Sonnenthal, E. L., Conrad, M. E., DePaolo, D. J., Gee, G. W., 2005. Multiphase
1023 reactive transport modeling of seasonal infiltration events and stable isotope fractionation
1024 in unsaturated zone pore water and vapor at the Hanford site. Vadose Zone J. 3, 775-785.
1025 Sonnenthal, E. L., Spycher, N., Apps, J. A., Simmons, A., 1998. Thermo-hydro-chemical
1026 predictive analysis for the drift-scale heater test. Lawrence Berkeley National Laboratory.
1027 Level 4 Milestone SPY289M4.
1028 Steefel, C. I., DePaolo, D. J., Lichtner, P. C., 2005. Reactive transport modeling: An essential
1029 tool and a new research approach for the Earth sciences. Earth Planet. Sci. Lett. 240, 539-
1030 558.
1031 Tardy, Y., Trauth, N., Krempp, G., 1972. Lithium in clay-minerals of sediments and soils.
1032 Geochim. Cosmochim. Acta 36, 397-&.
1033 Tardy, Y., Nahon, D., 1985. Geochemistry of laterites, stability of Al-goethite, Al-hematite, and
1034 Fe^{3+}-kaolinite in bauxites and ferricretes - an approach to the mechanism of concretion
1035 formation. Am. J. Sci. 285, 865-903.
1036 Teng, F.-Z., Rudnick, R. L., McDonough, W. F., Gao, S., Tomascak, P. B., Liu, Y., 2008.
1037 Lithium isotopic composition and concentration of the deep continental crust. Chem.
1038 Geol. 255, 47-59.
1039 Teng, F.-Z., Rudnick, R. L., McDonough, W. F., Wu, F.-Y., 2009. Lithium isotopic systematics
1040 of A-type granites and their mafic enclaves: Further constraints on the Li isotopic
1041 composition of the continental crust. Chem. Geol. 262, 370-379.
1042 Teng, F. Z., McDonough, W. F., Rudnick, R. L., Dalpé, C., Tomascak, P. B., Chappell, B. W.,
1043 Gao, S., 2004. Lithium isotopic composition and concentration of the upper continental
1044 crust. Geochim. Cosmochim. Acta 68, 4167-4178.
1045 Tipper, E. T., Calmels, D., Gaillardet, J., Louvat, P., Capmas, F., Dubacq, B., 2012. Positive
1046 correlation between Li and Mg isotope ratios in the river waters of the Mackenzie Basin
1047 challenges the interpretation of apparent isotopic fractionation during weathering. Earth
1048 Planet. Sci. Lett. 333–334, 35-45.
1049 Tomascak, P. B., Hemming, N. G., Hemming, S. R., 2003. The lithium isotopic composition of
1050 waters of the Mono Basin, California. Geochim. Cosmochim. Acta 67, 601-611.
1051 Vigier, N., Decarreau, A., Millot, R., Carignan, J., Petit, S., France-Lanord, C., 2008.
1052 Quantifying Li isotope fractionation during smectite formation and implications for the
1053 Li cycle. Geochim. Cosmochim. Acta 72, 780-792.
1054 Vigier, N., Gislason, S. R., Burton, K. W., Millot, R., Mokadem, F., 2009. The relationship
1055 between riverine lithium isotope composition and silicate weathering rates in Iceland.
1056 Earth Planet. Sci. Lett. 287, 434-441.

Voegelin, A. R., Nägler, T. F., Pettke, T., Neubert, N., Steinmann, M., Pourret, O., Villa, I. M., 2012. The impact of igneous bedrock weathering on the Mo isotopic composition of stream waters: Natural samples and laboratory experiments. Geochim. Cosmochim. Acta 86, 150-165.

Wanner, C., Sonnenthal, E. L., 2013. Assessing the control on the effective kinetic Cr isotope fractionation factor: A reactive transport modeling approach. Chem. Geol. 337, 88-98.

White, A. F., Bullen, T. D., Schulz, M. S., Blum, A. E., Huntington, T. G., Peters, N. E., 2001. Differential rates of feldspar weathering in granitic regoliths. Geochim. Cosmochim. Acta 65, 847-869.

White, A. F., 2002. Determining mineral weathering rates based on solid and solute weathering gradients and velocities: application to biotite weathering in saprolites. Chem. Geol. 190, 69-89.

Wimpenny, J., Gislason, S. R., James, R. H., Gannoun, A., Pogge Von Strandmann, P. A. E., Burton, K. W., 2010. The behaviour of Li and Mg isotopes during primary phase dissolution and secondary mineral formation in basalt. Geochim. Cosmochim. Acta 74, 5259-5279.

Wimpenny, J., James, R. H., Burton, K. W., Gannoun, A., Mokadem, F., Gíslason, S. R., 2010b. Glacial effects on weathering processes: New insights from the elemental and lithium isotopic composition of West Greenland rivers. Earth Planet. Sci. Lett. 290, 427-437.

Wimpenny, J., Colla, C. A., Yin, Q.-Z., Rustad, J. R., Casey, W. H., 2014. Investigating the behaviour of Mg isotopes during the formation of clay minerals. Geochim. Cosmochim. Acta 128, 178-194.

Xu, T., Spycher, N., Sonnenthal, E. L., Zhang, G., Zheng, L., Pruess, K., 2011. TOUGHREACT Version 2.0: A simulator for subsurface reactive transport under non-isothermal multiphase flow conditions. Comput. Geosci. 37, 763-774.

Yang, L., Steefel, C. I., 2008. Kaolinite dissolution and precipitation kinetics at 22°C and pH 4. Geochim. Cosmochim. Acta 72, 99-116.

Yoon, J., 2010. Lithium as a Silicate Weathering Proxy: Problems and Perspectives. Aquatic Geochemistry 16, 189-206.

Zhang, L., Chan, L.-H., Gieskes, J. M., 1998. Lithium isotope geochemistry of pore waters from ocean drilling program Sites 918 and 919, Irminger Basin. Geochim. Cosmochim. Acta 62, 2437-2450.

Ziegler, K., Chadwick, O. A., Brzezinski, M. A., Kelly, E. F., 2005. Natural variations of $\delta^{30}Si$ ratios during progressive basalt weathering, Hawaiian Islands. Geochim. Cosmochim. Acta 69, 4597-4610.

Figure 1
Click here to download high resolution image

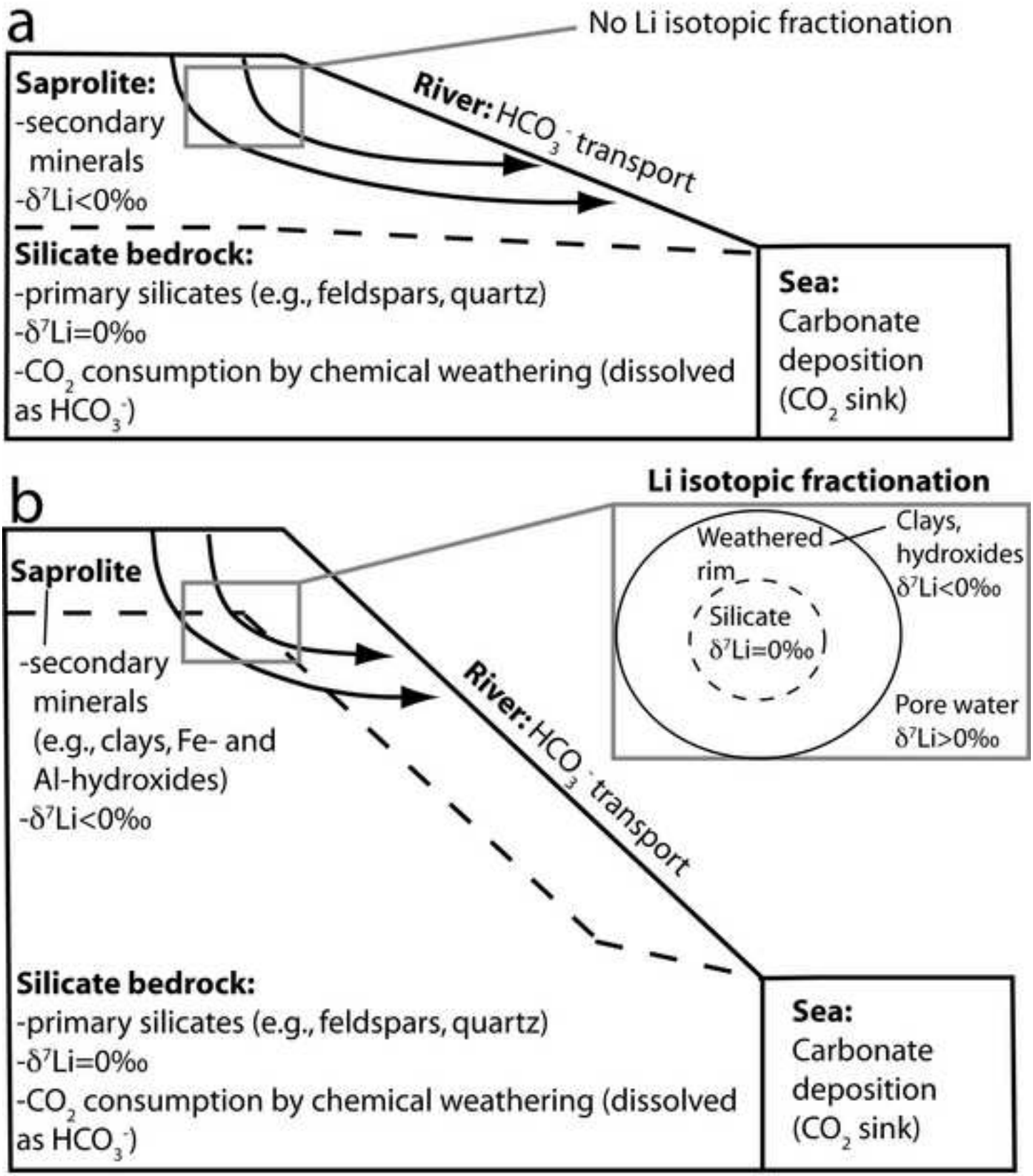

Figure 2

Click here to download high resolution image

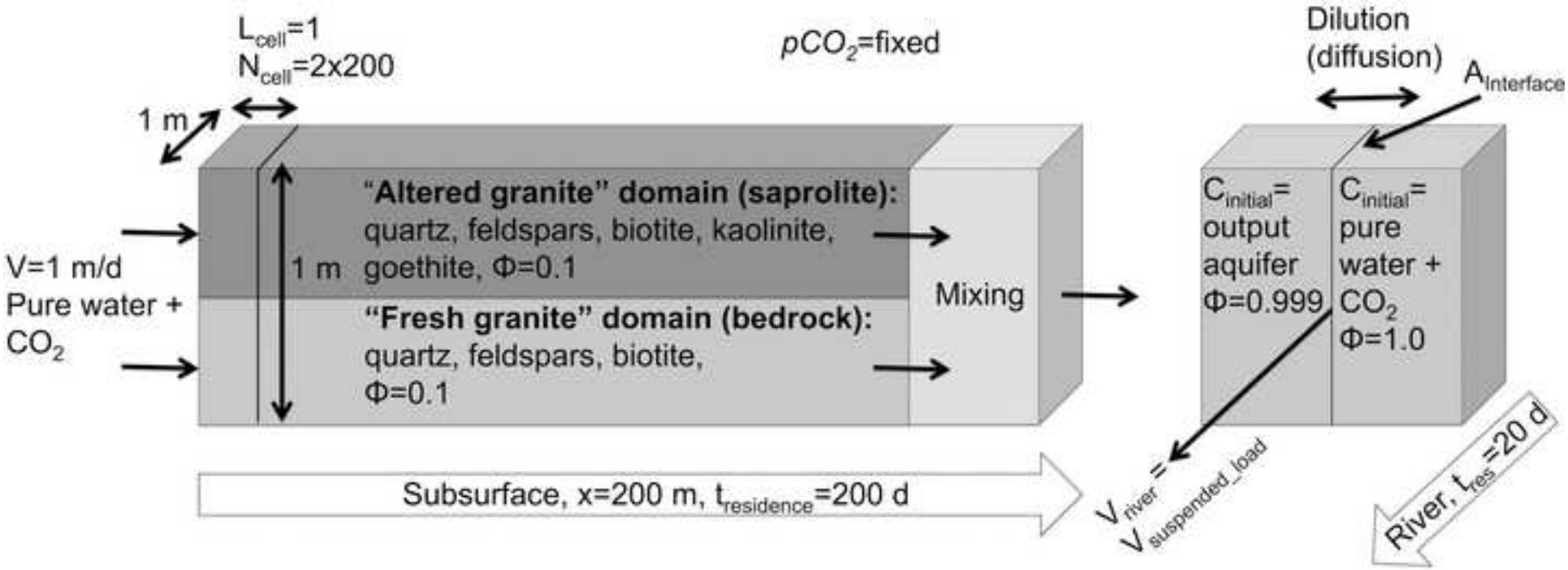

Figure 3
Click here to download high resolution image

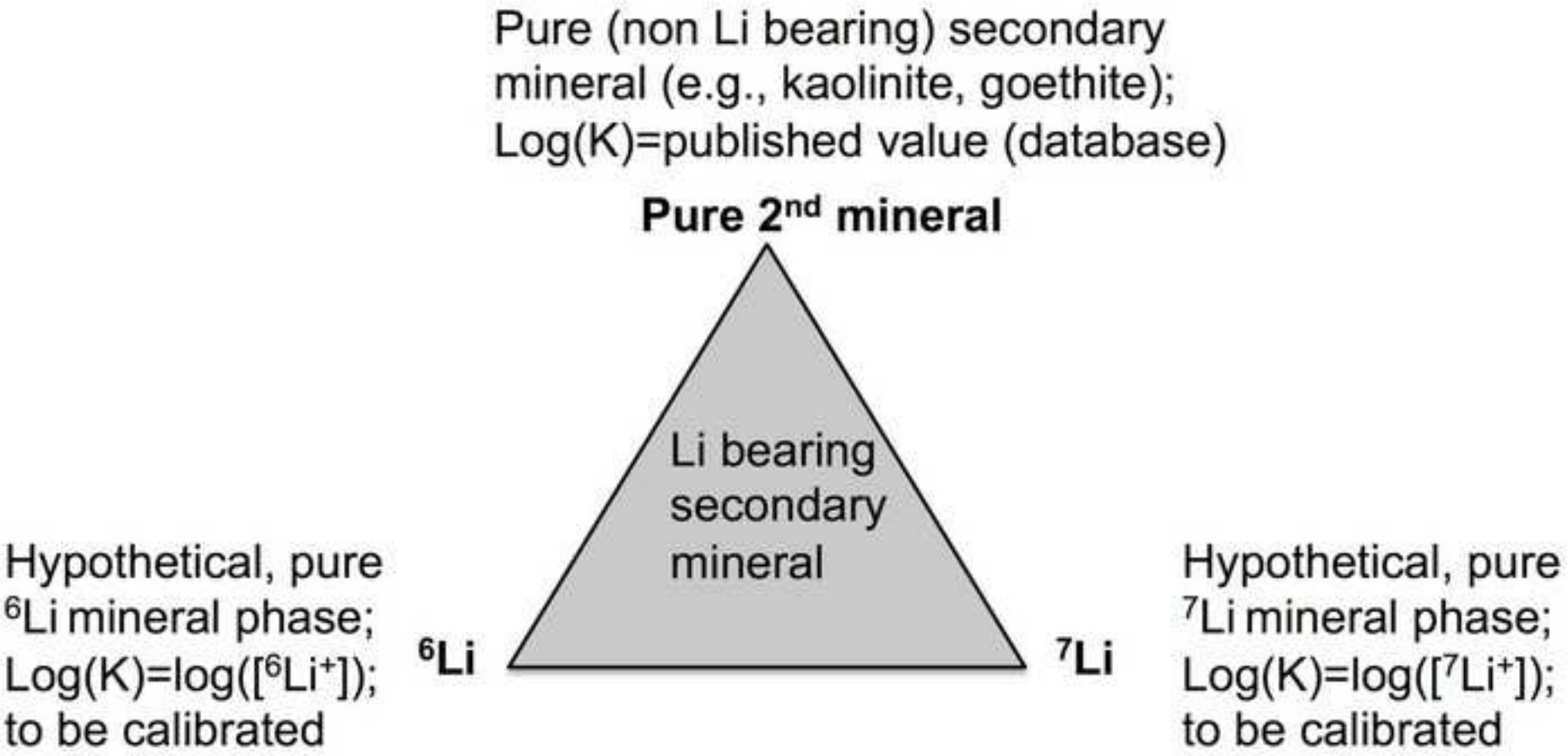

Figure 4

Click here to download high resolution image

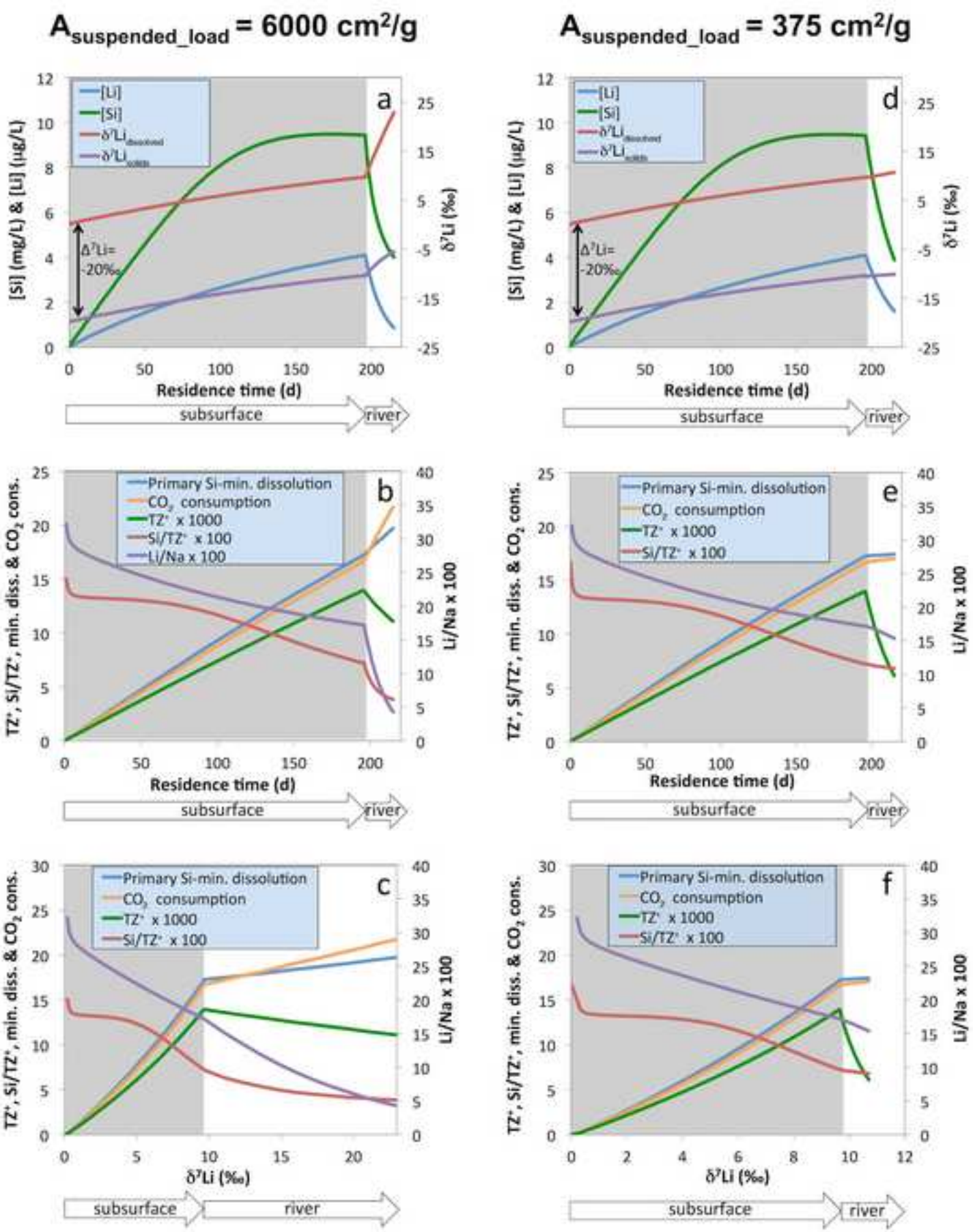

Figure 5

Click here to download high resolution image

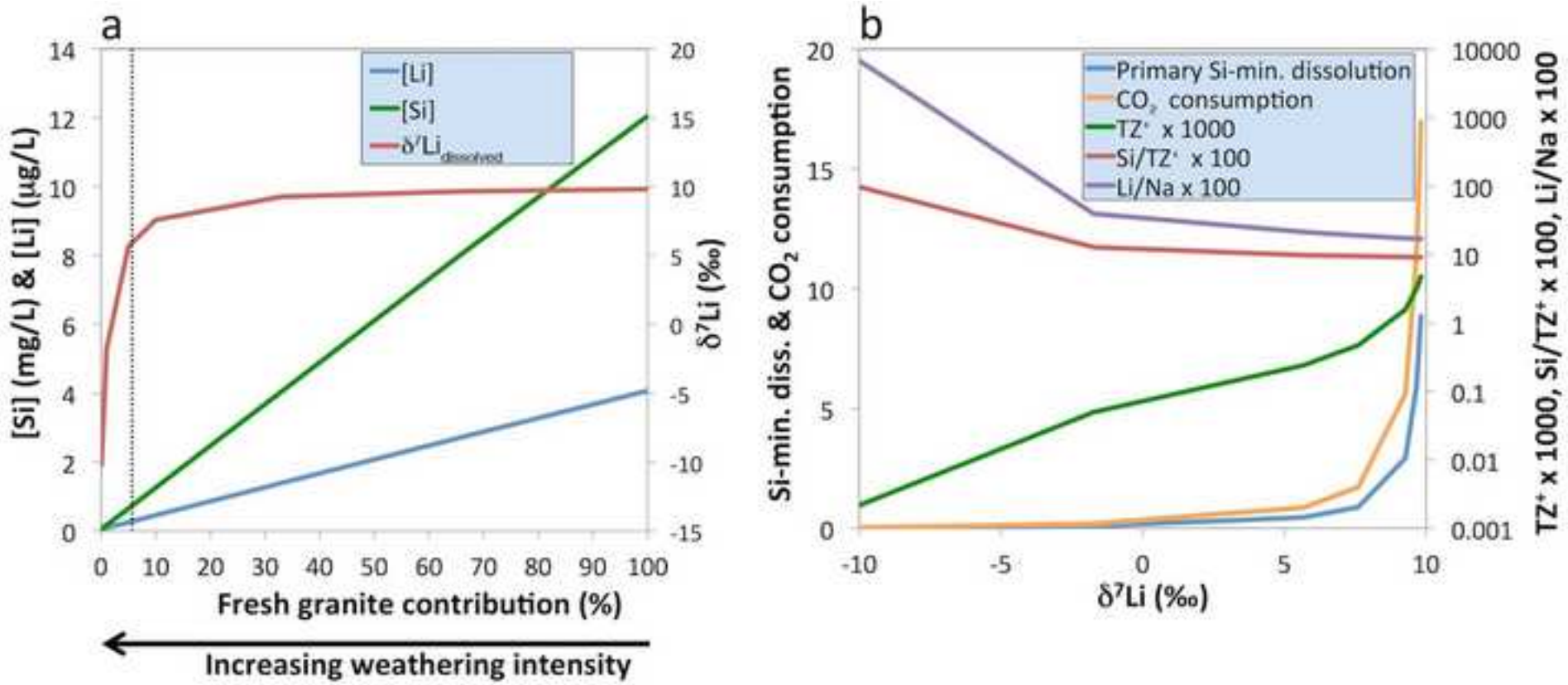

Figure 6

Click here to download high resolution image

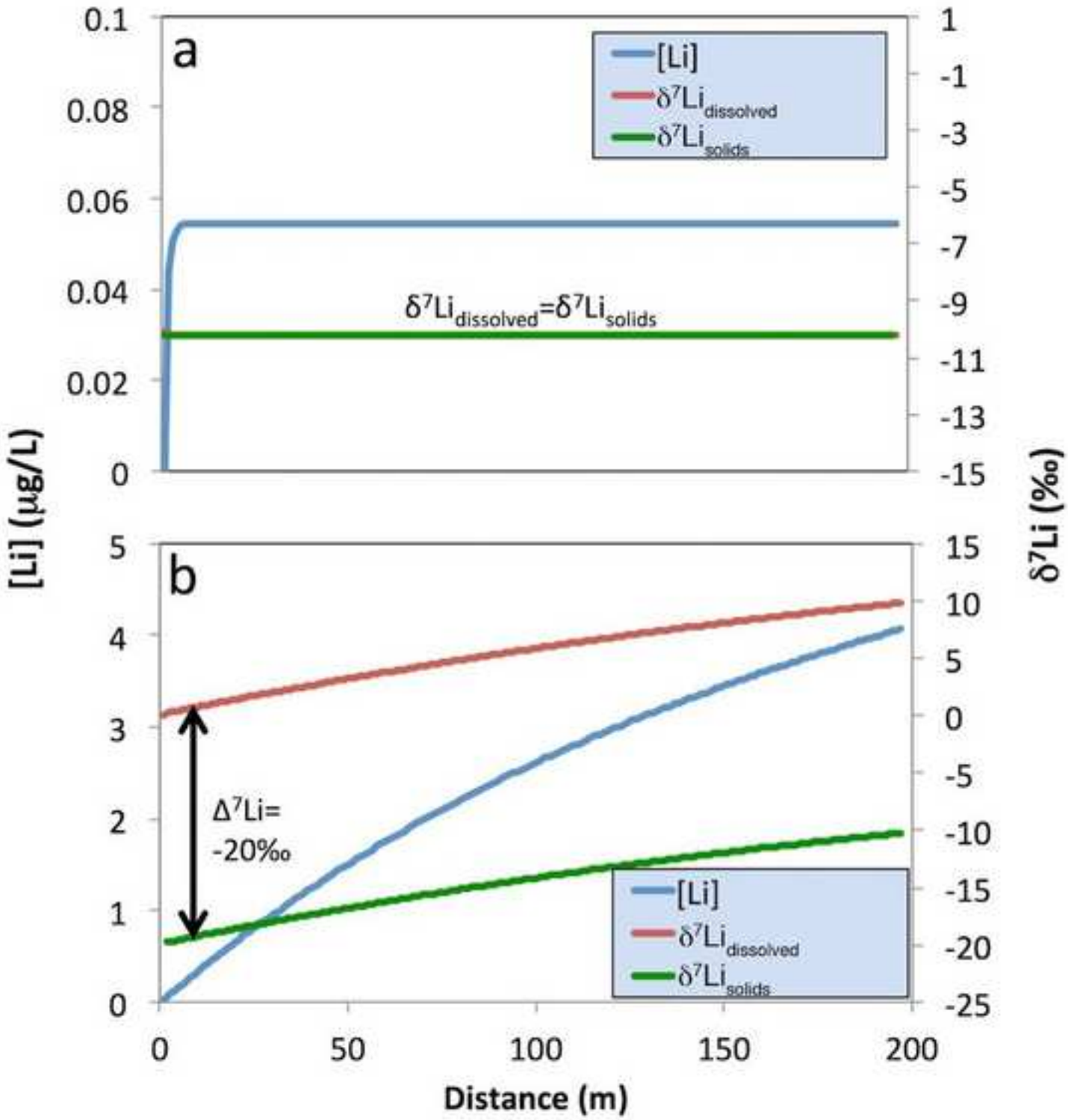

Figure 7

Click here to download high resolution image

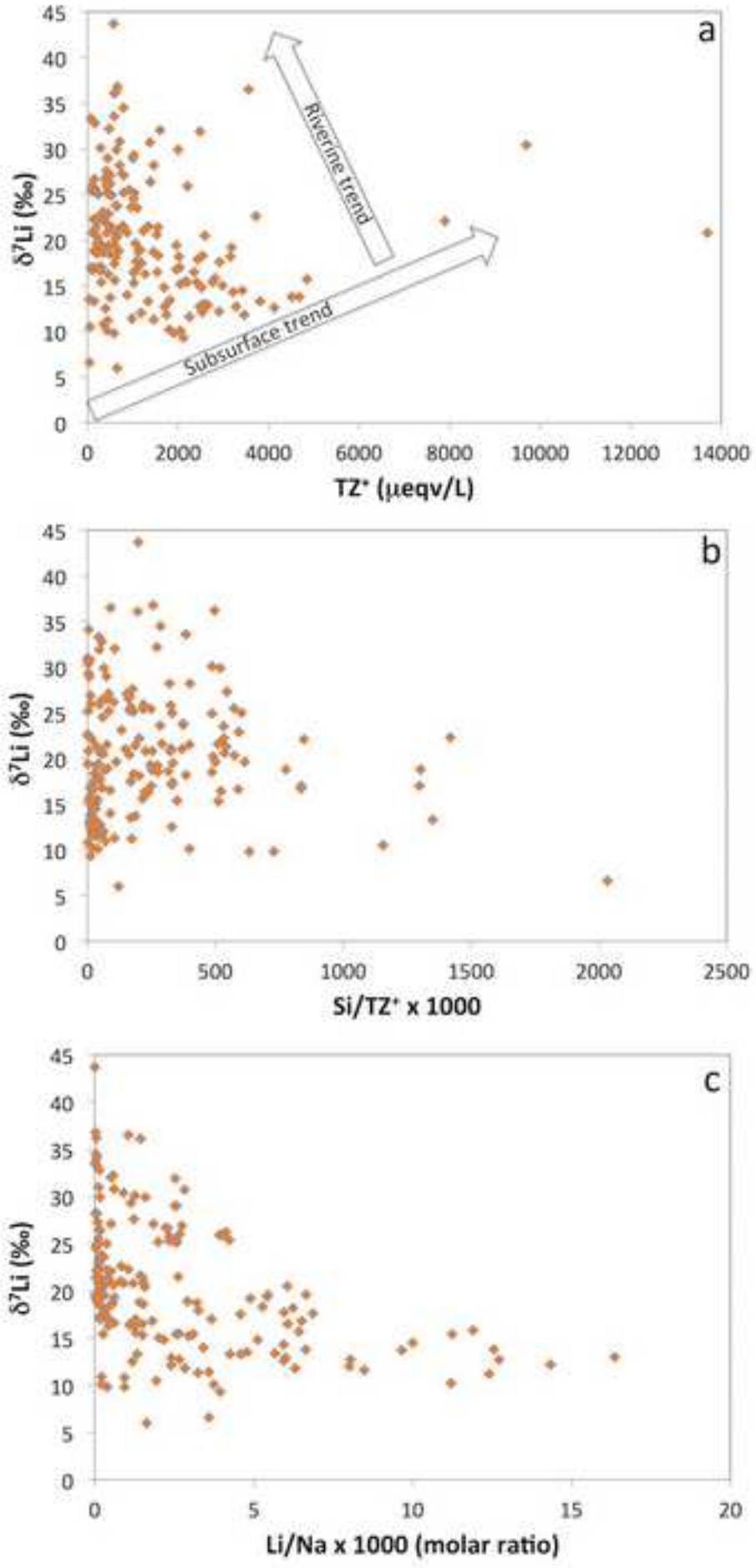

Table 1+2

Click here to download Table: Tables.docx

TABLE 1. INITIAL AND BOUNDARY CONDITIONS

		Simulation of current weathering pattern		Simulation of Paleocene-Eocene boundary weathering pattern	
		subsurface	river	"Fresh Granite"	"Altered Granite"
pH	-	5.63	[d]8.79	5.37	5.37
HCO_3^-	mol/kgH_2O	[a]1.51E-5	[d]4.18E-3	[b]4.52E-05	[b]4.52E-05
Na^+	mol/kgH_2O	1.0E-10	[d]3.45E-6	1.0E-10	1.0E-10
K^+	mol/kgH_2O	1.0E-10	[d]1.67E-4	1.0E-10	1.0E-10
Mg^{2+}	mol/kgH_2O	1.0E-10	[d]2.00E-5	1.0E-10	1.0E-10
Ca^{2+}	mol/kgH_2O	1.0E-10	[d]2.22E-3	1.0E-10	1.0E-10
Al^{3+}	mol/kgH_2O	1.0E-10	[d]8.31E-7	1.0E-10	1.0E-10
$^6Li^+$	mol/kgH_2O	[c]7.68095e-11	[d]4.5097E-8	[c]7.68095e-11	[c]7.68095e-11
$^7Li^+$	mol/kgH_2O	[c]9.23191E-10	[d]5.4726E-7	[c]9.23191E-10	[c]9.23191E-10
$SiO_{2(aq)}$	mol/kgH_2O	1.0E-10	[d]3.36E-4	1.0E-10	1.0E-10
$O_{2(aq)}$	mol/kgH_2O	2.5E-4	2.5E-4	2.5E-4	2.5E-4
Fe^{2+}	mol/kgH_2O	1.0E-10	[d]6.59E-19	1.0E-10	1.0E-10
$CO_{2(s)}$	vol frac (of solids)	0.01	0.01	0.01	0.01
Albite	vol frac (of solids)	0.304	0.304	0.304	0.304
Anorthite	vol frac (of solids)	0.076	0.076	0.076	0.076
Orthoclase	vol frac (of solids)	0.29	0.29	0.29	0.29
Quartz	vol frac (of solids)	0.31	0.31	0.31	0.31
Annite	vol frac (of solids)	0.04	0.04	0.04	0.04
Li-phlogopite	vol frac (of solids)	0.01	0.01	0.01	0.01
Kaolinite	vol frac (of solids)	0.0	0.0	0.0	0.004[e]
^6Li (kaolinite)	vol frac (of solids)	0.0	0.0	0.0	0.00031020[e]
^7Li (kaolinite)	vol frac (of solids)	0.0	0.0	0.0	0.00368979[e]
Goethite	vol frac (of solids)	0.0	0.0	0.0	0.0003[e]
^6Li (kaolinite)	vol frac (of solids)	0.0	0.0	0.0	0.00002326[e]
^7Li (kaolinite)	vol frac (of solids)	0.0	0.0	0.0	0.00027673[e]
Porosity	-	0.1	0.99	0.1	0.1

[a]Calculated by assuming equilibrium with pCO_2 of 370 ppmV (log(pCO_2)=-3.43)
[b]Calculated by assuming equilibrium with pCO_2 of 1200 ppmV (log(pCO_2)=-2.92)
[c]Specification corresponds to an initial δ^7Li of 0.0‰
[d]Read out from downstream boundary of aquifer model run
[e]Read out from model run with "fresh granite" domain only

Table 2. SIMULATED SILICATE WEATHERING REACTIONS

Mineral phase	[e]log(K)	[f]k (mol/m^2/s)	[g]A "fresh granite" (cm^2/g)	A "altered granite" (cm^2/g)	A "river simulation" (cm^2/g)	Hydrolysis reaction
$CO_{2(s)}$[a]	-11.25	1.00e-04	100	100	100	$CO_{2(s)} + H_2O = H^+ + HCO_3^-$
Albite[c1]	1.41	2.75e-13	1	0	6000 or 375[h]	$NaAlSi_3O_8 + 4H^+ = Na^+ + 3SiO_{2(aq)} + Al^{3+} + 2H_2O$
Anorthite[c1]	24.52	7.59e-10	1	0	6000 or 375	$CaAl_2Si_2O_8 + 8H^+ = Ca^{2+} + 2SiO_{2(aq)} + 3Al^{3+} + 4H_2O$
Orthoclase	-0.20	3.89E-13	1	0	6000 or 375	$KAlSi_3O_8 + 4H^+ = K^+ + 3SiO_{2(aq)} + Al^{3+} + 2H_2O$
Quartz	-4.05	2.46e-13	1	0	6000 or 375	$SiO_{2(s)} = SiO_{2(aq)}$
Annite[c2]	18.31	7.76e-12	2.4	0	6000 or 375	$FeCaSi_2O_6 + 4H^+ = Ca^{2+} + Fe^{2+} + 2SiO_{2(aq)} + 2H_2O$
Li-phlogopite[b,c2]	37.428	2.82E-13	2.4	0	6000 or 375	$K_{1.144}Mg_{2.856}Li_{0.144}(AlSi_3O_{10})(OH)_2 + 10H^+ = 1.144K^+ + 2.856\ Mg^{2+} + 0.01104322\ {}^6Li^+ + 0.13295678\ {}^7Li^+ + Al^{3+} + 3SiO_{2(aq)}$
Kaolinite[S3]	7.55	6.6e-14	6824	6824	6000 or 375	$Al_2Si_2O_5(OH)_4 + 6H^+ = 2Al^{3+} + 2SiO_{2(aq)} + 5H_2O$
^{6}Li (Kaolinite)[d, c3]	-2.60877392	6.6e-14	6824	6824	6000 or 375	$^6Li = {}^6Li^+$
^{7}Li(Kaolinite)[d, c3]	-2.6	6.6e-14	6824	6824	6000 or 375	$^7Li = {}^7Li^+$
Goethite[S4]	-8.3710	1.15e-8	6824	6824	6000 or 375	$Fe(OH)_3 + 2H^+ = 0.25O_{2(aq)} + 1.5H_2O + 1Fe^{2+}$
^{6}Li (Goethite)[d, c4]	-2.60877392	1.15e-8	6824	6824	6000 or 375	$^6Li = {}^6Li^+$
^{7}Li (Goethite)[d, c4]	-2.6	1.15e-8	6824	6824	6000 or 375	$^7Li = {}^7Li^+$

[a]Hypothetical solid $CO_{(s)}$ phase to fix pCO_2 (= model CO_2 source). Different values were defined to fix pCO_2 to 1200 ppmV (log(K)=-10.739) and 370ppmV (log(K)=-11.252)
[b]Corresponds to a phlogopite Li concentration of 2400 ppm to get an initial bulk granite Li conc. of 24 ppm according to Economos (2009) (at a phlogopite vol fraction of 0.01), and a δ^7Li value of 0.0 ‰
[cx]Endmbember of solid solution x.
[d]Li isotopic endmember of defined solid solution (Fig. 3). K_{6Li}/K_{7Li}= 0.98=$\Delta^7Li_{solution\text{-}kaolinite}$ =-20‰. Log(K) was calibrated to get maximum Li concentration in goethite and kaolinite of about 200 ppm.
[e]With the exception of kaolinite, which was defined according to Yang and Steefel (2008), equilibrium constants log(*K*) were defined according to Reed and Palandri (2006).
[f]Reaction rate constants *k* were defined according to Palandri & Kharaka (2006)
[g]Reactive surface areas of primary silicate minerals (feldspars, quartz, biotite) were calibrated to get a Li concentration larger than the global average riverine Li conc. (0.265 μmol/L) at the downstream aquifer model boundary ("mixing", Fig. 2). Reactive surface areas of secondary minerals (e.g., kaolinite, goethite) were set to 6824 cm^2/g according to Dobson et al. (2003).
[h]River simulations were run for two different reactive surface area to simulate the effects of a varying suspended river load on riverine δ^7Li values. 6000 cm2/g allowed matching the current global average riverine δ^7Li values after a simulated river residence time of 20 d.